Pergamon

Int. J. Solids Structures Vol. 35, No. 36, pp. 5205–5236, 1998

Printed in Great Britain
0020–7683/98/$—see front matter

PII: S0020–7683(97)00265–5

TEXTURE DEVELOPMENT AND PLASTIC ANISOTROPY OF B.C.C. STRAIN HARDENING SHEET METALS

K.-C. LIAO
Mechanical Engineering and Applied Mechanics, The University of Michigan, Ann Arbor MI 48109, U.S.A.

P. A. FRIEDMAN
Ford Motor Company, Dearborn MI 48121, U.S.A.

J. PAN*
Mechanical Engineering and Applied Mechanics, The University of Michigan, Ann Arbor MI 48109, U.S.A.

and

S. C. TANG
Ford Motor Company, Dearborn MI 48121, U.S.A.

(*Received* 6 *May* 1997; *in revised form* 1 *September* 1997)

Abstract—A Taylor-like polycrystal model is adopted here to investigate the plastic behavior of body centered cubic (b.c.c.) sheet metals under plane-strain compression and the subsequent in-plane biaxial stretching conditions. The ⟨111⟩ pencil glide system is chosen for the slip mechanism for b.c.c. sheet metals. The {110} ⟨111⟩ and {112} ⟨111⟩ slip systems are also considered. Plane-strain compression is used to simulate the cold rolling processes of a low-carbon steel sheet. Based on the polycrystal model, pole figures for the sheet metal after plane-strain compression are obtained and compared with the corresponding experimental results. Also, the simulated plane-strain stress–strain relations are compared with the corresponding experimental results. For the sheet metal subjected to the subsequent in-plane biaxial stretching and shear, plastic potential surfaces are determined at a given small amount of plastic work. With the assumption of the equivalence of the plastic potential and the yield function with normality flow, the yield surfaces based on the simulations for the sheet metal are compared with those based on several phenomenological planar anisotropic yield criteria. The effects of the slip system and the magnitude of plastic work on the shape and size of the yield surfaces are shown. The plastic anisotropy of the sheet metal is investigated in terms of the uniaxial yield stresses in different planar orientations and the corresponding values of the anisotropy parameter R, defined as the ratio of the width plastic strain rate to the through-thickness plastic strain rate under in-plane uniaxial tensile loading. The uniaxial yield stresses and the values of R at different planar orientations from the polycrystal model can be fitted well by a yield function recently proposed by Barlat *et al.* (1997b).

1. INTRODUCTION

Sheet metals often display significant plastic anisotropy after manufacturing processes such as cold or hot rolling. These sheet metals usually exhibit not only normal anisotropy but also planar anisotropy. For metals, the primary source of plastic anisotropy up to moderately large strains comes from the texture or the preferred crystallographic orientations of the grains. The plastic anisotropic properties of sheet metals have generally been investigated by two approaches. The first one is to develop various macroscopic yield functions from a phenomenological viewpoint. The second approach is to develop polycrystal models based on the constitutive behavior of crystalline slip in single crystals.

*Author to whom correspondence should be addressed. Tel.: 001 734 764 9404. Fax: 001 734 647 3170. E-mail: jwo@engin.umich.edu.

Many phenomenological yield criteria were proposed in the past to account for plastic anisotropy. Hill's quadratic yield criterion (1948) has been widely used. In recent years, non-quadratic yield criteria have received much attention (for example, see Lee *et al.*, 1996). An excellent review on plastic anisotropy can be found in Hosford (1996). However, neither Hill's quadratic yield criterion (1948) nor Hosford's non-quadratic yield criterion (1979) can encompass the so-called anomalous behavior of some metals. Hill (1979) modified his quadratic criterion to encompass some observed anomalous behaviors. However, Hill's new criteria are constrained by the requirement that the principal stress axes and the anisotropic symmetry axes be in the same directions. These criteria cannot be used to describe any state involving shear stresses with respect to these axes. Gotoh (1977) suggested a fourth-order polynomial criterion which does not have the limitation mentioned above. However, the yield criterion contains nine undetermined constants even under plane stress conditions and is therefore too complicated for use in practice.

Barlat and Lian (1989) and Barlat *et al.* (1991) proposed a tricomponent and a six-component yield criterion, respectively. The shapes of the yield surfaces based on these yield criteria agree well with those of the upper-bound solutions based on the polycrystal model of Taylor (1938) and Bishop and Hill (1951a, b) using the texture data for aluminum alloys. This is especially seen near the equal biaxial loading direction where the yield surfaces of the criteria with high values of the exponents lead to some rounded vertices similar to the experimental results. Recently, Barlat *et al.* (1997a, b) modified the six-component yield criterion (Barlat *et al.*, 1991) to improve the prediction of the yield surfaces when compared with experimental results.

Hill (1990) developed an improved plane-stress yield criterion for orthotropic sheet metals. The criterion can be used to account for the orientation dependence when the orthotropy axes and the principal stress directions do not coincide with each other. Lin and Ding (1996) modified Hill's yield criterion (1990) without imposing additional mathematical complexities. Lin and Ding (1996) showed that the yield surface based on the modified Hill's yield criterion becomes closer to the experimental results. Hill (1993) also proposed a user-friendly yield criterion for orthotropic sheet metals. Included in this criterion is a particular pair of cubic terms into his original quadratic yield criterion (1948) to describe the yield stress and the anisotropy parameter R in the rolling and transverse directions as well as the equal biaxial yield stress. Here, the anisotropy parameter R is defined as the ratio of the width plastic strain rate to the through-thickness plastic strain rate under in-plane uniaxial tensile loading. One major concern of all the yield criteria reviewed above is that the evolution of texture under non-proportional loading conditions cannot easily be accounted for.

From a microscopic viewpoint, slip in a certain preferred direction on a certain preferred plane is the main mechanism of plastic deformation at low homologous temperature. If the constitutive behavior of each grain based on crystalline slip is available, then the transition from the microscopic response of an individual grain to the macroscopic response of the aggregate can be obtained via some averaging schemes. The advantage of this approach is that the constitutive behavior can be simulated under any loading path once the constitutive parameters of slip processes and the initial distribution of grain orientations of a workpiece are known. The initial texture of the workpiece can be obtained from X-ray diffraction analyses or by computational simulations of manufacturing processes. However, in this approach, a substantial amount of computational time is still needed for even a workpiece of simple geometry under simple loading conditions such as uniaxial tension or compression.

For f.c.c. aluminum alloys, recent studies on yield surfaces can be found, for example, in Asaro and Needleman (1985), Lin and Ding (1996), Yang and Bacroix (1996) and Barlat *et al.* (1997a, b). For b.c.c. metals, studies on plastic behavior and texture can be found, for example, in Gilormini (1989) and Ceccaldi *et al.* (1994). For b.c.c. metals, Taylor (1955) suggested the $\langle 111 \rangle$ pencil glide system such that slip can occur on any plane associated with any of the four $\langle 111 \rangle$ slip directions. Hutchinson (1964) approximated the pencil glide by assuming slip on any of a large but finite number of planes containing the $\langle 111 \rangle$ slip directions. Examining all possible independent combinations of five such slip systems,

Hutchinson selected the one having the minimum plastic work. He used this procedure to calculate the yield surface for a randomly oriented polycrystal. Logan and Hosford (1980) investigated the yield surfaces for several rotationally symmetrical textured sheet metals based on an upper-bound model and the $\langle 111 \rangle$ pencil glide system.

As computational simulations of sheet forming processes become necessary for fast product development, more accurate yield criteria and constitutive models are needed. In fact, finite element simulations of forming processes based on the polycrystal model of Asaro and Needleman (1985) have been performed by Mathur and Dawson (1989), Kalidindi *et al.* (1992), Becker (1993), Baudoin *et al.* (1994) and Baudoin *et al.* (1996). However, the computational time is prohibitively high for these simulations. Although there have been many experimental and analytical studies performed on f.c.c. metals (for example, see Barlat *et al.*, 1997a, b), there is a lack of a thorough experimental and analytical study for b.c.c. metals. Therefore, in this study, we examine the plastic behavior of b.c.c. low-carbon steels.

It should be noted that the yield surface, determined at a given amount of plastic work, for any loading paths that cause substantial texture change, is not the yield surface of the given texture. Asaro and Needleman (1985) determined their reference yield surfaces at the Mises effective strains of 0.2%, 0.1% and 0.05% whereas Lin and Ding (1996) determined their yield surfaces at the Mises effective strain of 0.2%. Barlat *et al.* (1997a) determined their yield surfaces at the plastic work of approximately a plastic strain of 10%. In this work, we determine the reference yield surfaces at small amounts of plastic work equivalent to those of the uniaxial tensile strain of 0.2% and 0.02% in the rolling direction to understand the relations between the yield (or work) surfaces and the phenomenological yield surfaces for b.c.c. metals. In addition, we understand that for f.c.c. metals, the texture data were used to obtain upper-bound solutions which, in general, agree well with the yield criterion (Barlat and Lian, 1989). However, the deformation history or hardening effect on plastic behavior under non-proportional loading conditions cannot be accounted for by upper-bound analyses. Therefore, in this work, we concentrate on this deformation history and hardening effects on the plastic behavior of b.c.c. metals.

The outline of this paper is as follows. First, a Taylor-like polycrystal model of Asaro and Needleman (1985) is briefly reviewed for convenient presentation of our implementation of different slip systems for b.c.c. metals into their polycrystal model. Then, the deformation kinematics of single crystals and the constitutive relation for the nominal stress rate and the deformation gradient rate of single crystals as well as the aggregate are reviewed. In Section 3, the computational procedures of the polycrystal model are briefly summarized. In Section 4, both the stress–strain response and the crystallographic texture of a low-carbon steel sheet metal based on the polycrystal model under plane-strain compressive loading conditions are obtained and compared with those of the corresponding experiments (Friedman *et al.*, 1997). Based on the polycrystal model with the $\langle 111 \rangle$ pencil glide system as well as two other possible slip systems for b.c.c. metals, macroscopic yield (or work) surfaces projected on the in-plane normal stress plane for both initially isotropic and textured sheet metals are obtained. The yield surfaces based on the polycrystal model are compared with those of several available phenomenological anisotropic yield criteria. The plastic anisotropy of the sheet metal subjected to the subsequent in-plane loading is investigated by the uniaxial yield stresses and the corresponding anisotropy parameter R at different planar orientations. Finally, some conclusions are made.

2. A POLYCRYSTAL MODEL

Among various polycrystal models, we adopt a Taylor-like model developed by Asaro and Needleman (1985) for polycrystals subjected to arbitrarily large strains. The fundamental assumption of their model is exactly the same as that of the well-known Taylor model with the strain field in each grain being assumed to be homogeneous and the same as that of the aggregate. Therefore, compatibility is satisfied and equilibrium holds in each grain. However, equilibrium may be violated between grains. The mechanism of the plastic deformation considered here is the crystalline slips in certain preferred directions on certain

preferred planes. Twinning, cross slip or grain boundary sliding are excluded. Neither Bauschinger effect nor temperature effect is considered here. Each grain in the aggregate is assumed to have the same volume fraction and maintain cubical symmetry during plastic deformation.

2.1. *Kinematics of crystalline deformation*

The deformation characteristics of each grain follow the kinematic formulation for single crystals as described in Asaro and Rice (1977) and Asaro and Needleman (1985). The material is first assumed to flow through the crystal lattice due to plastic shearing followed by elastic deformation and rigid body rotation of the lattice. For simplicity, the slip process of only one slip system is schematically plotted in Fig. 1. In the figure, $\mathbf{s}^{(\alpha)}$ stands for the unit vector in the slip direction lying on the slip plane and $\mathbf{m}^{(\alpha)}$ stands for the unit normal vector perpendicular to the corresponding slip plane in the undeformed configuration. Here a superscript α indicates the αth slip system. In general, the deformation gradient of a single crystal, $\mathbf{F}$, can be multiplicatively decomposed (Lee, 1969) in the form of

$$\mathbf{F} = \mathbf{F}^* \cdot \mathbf{F}^p, \tag{1}$$

where $\mathbf{F}^p$ includes the plastic shearing on the slip planes inducing no change of vectors $\mathbf{s}^{(\alpha)}$ and $\mathbf{m}^{(\alpha)}$ where $\mathbf{F}^*$ deals with the elastic distortion and rigid body rotation of the crystal lattice.

For the deformed lattice, the slip direction vector and the slip plane normal vector corresponding to the αth slip system become

$$\mathbf{s}^{*(\alpha)} = \mathbf{F}^* \cdot \mathbf{s}^{(\alpha)} \tag{2}$$

$$\mathbf{m}^{*(\alpha)} = \mathbf{m}^{(\alpha)} \cdot \mathbf{F}^{*-1}, \tag{3}$$

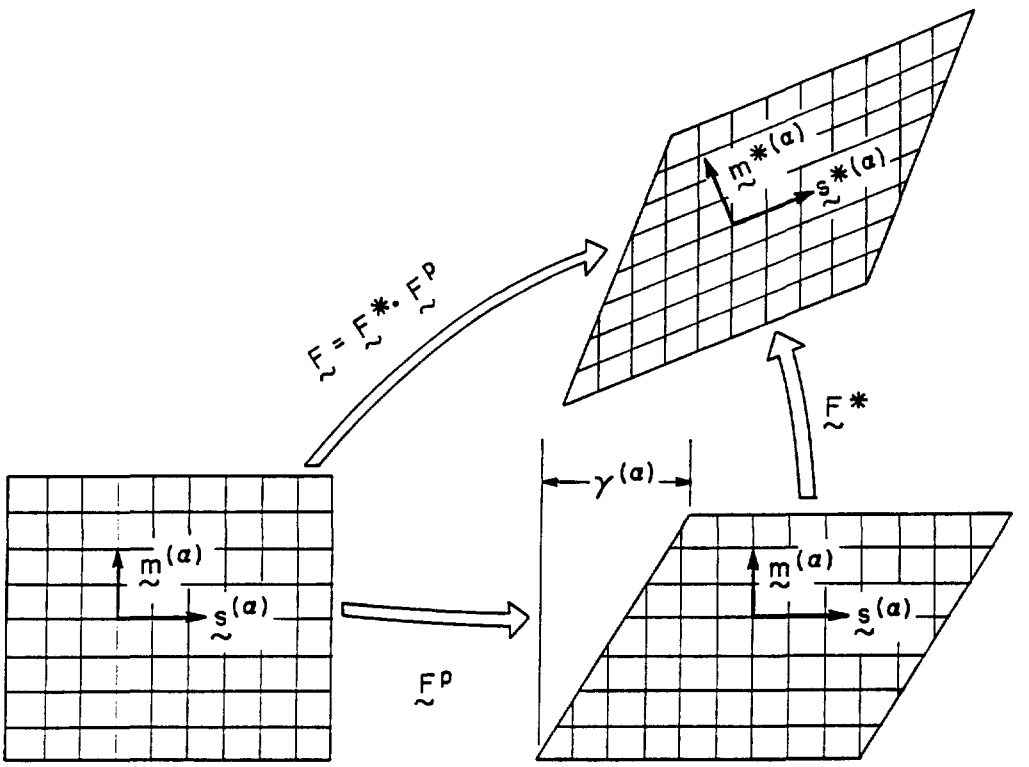

Fig. 1. Representation of deformation of a single crystal under a single slip.

where $(\cdot)^{-1}$ represents the inverse of $(\cdot)$. Here, $\mathbf{m}^{*(\alpha)}$ is obtained by the cross product of two vectors lying on the αth slip plane.

The spatial gradient of the velocity is defined as

$$\dot{\mathbf{F}} \cdot \mathbf{F}^{-1} = \mathbf{D} + \boldsymbol{\Omega}, \tag{4}$$

where the deformation rate $\mathbf{D}$ and the spin rate $\boldsymbol{\Omega}$ are the symmetric and the anti-symmetric part of $\dot{\mathbf{F}} \cdot \mathbf{F}^{-1}$, respectively. Also, $\mathbf{D}$ and $\boldsymbol{\Omega}$ can be composed into the sum of the corresponding rates based on the plastic shearing and those based on the crystal lattice deformation as

$$\mathbf{D} = \mathbf{D}^* + \mathbf{D}^p \tag{5}$$

$$\boldsymbol{\Omega} = \boldsymbol{\Omega}^* + \boldsymbol{\Omega}^p. \tag{6}$$

The plastic part of the spatial gradient of the velocity arisen from the deformed slip systems $(\mathbf{s}^{*(\alpha)}, \mathbf{m}^{*(\alpha)})$ can be expressed as

$$\dot{\mathbf{F}} \cdot \mathbf{F}^{-1} - \dot{\mathbf{F}}^* \cdot \mathbf{F}^{*-1} = \mathbf{D}^p + \boldsymbol{\Omega}^p = \sum_{\alpha} \dot{\gamma}^{(\alpha)} \mathbf{s}^{*(\alpha)} \mathbf{m}^{*(\alpha)}, \tag{7}$$

where $\dot{\gamma}^{(\alpha)}$ represents the shear strain rate on the αth slip system, and $\mathbf{D}^p$ and $\boldsymbol{\Omega}^p$ are the symmetric and the anti-symmetric part of the right hand side of eqn (7), respectively.

2.2. *Constitutive relation*

The constitutive response of a single crystal is established by an assumption that the second Piola–Kirchhoff stress $\mathbf{T}^*$ for the lattice distortion can be derived from the lattice strain energy per unit reference volume, ϕ, and the Lagrangian strain of the lattice, $\mathbf{E}^*$, as

$$\mathbf{T}^* = \frac{\partial \phi}{\partial \mathbf{E}^*}. \tag{8}$$

The rate of the lattice-based second Piola–Kirchhoff stress can be expressed as

$$\dot{\mathbf{T}}^* = \frac{\partial^2 \phi}{\partial \mathbf{E}^* \, \partial \mathbf{E}^*} : \quad \dot{\mathbf{E}}^* = \mathscr{D} : \dot{\mathbf{E}}^* \tag{9}$$

where $\mathscr{D}$ is the elastic moduli for a cubically symmetric crystal. When the orthogonal coordinate axes are chosen to be coincided with the cubic axes of a grain, three independent nonzero components of the elastic moduli are

$$\begin{aligned} \mathscr{D}_{iiii} &= C_{11} \quad \text{(no summation)} \\ \mathscr{D}_{iijj} &= C_{12} \quad \text{for } i \neq j \quad \text{(no summation)} \\ \mathscr{D}_{ijij} = \mathscr{D}_{ijji} &= C_{44} \quad \text{for } i \neq j \quad \text{(no summation)}, \end{aligned} \tag{10}$$

where C_{11}, C_{12}, and C_{44} are the elastic material constants. Here the Roman subscripts have a range of 1 to 3.

The Kirchhoff stress $\boldsymbol{\tau}$ can be related to the lattice-based second Piola–Kirchhoff stress $\mathbf{T}^*$ as

$$\boldsymbol{\tau} = \mathbf{F}^* \cdot \mathbf{T}^* \cdot \mathbf{F}^{*T}, \tag{11}$$

where $(\cdot)^T$ represents the transpose of $(\cdot)$. Then eqns (9) and (11) are used to derive the rate of the Kirchhoff stress as

$$\dot{\boldsymbol{\tau}} = \mathbf{F}^* \cdot (\mathscr{D} : \dot{\mathbf{E}}^*) \cdot \mathbf{F}^{*T} + \dot{\mathbf{F}}^* \cdot \mathbf{F}^{*-1} \cdot \boldsymbol{\tau} + \boldsymbol{\tau} \cdot \mathbf{F}^{*-T} \cdot \dot{\mathbf{F}}^{*T}, \tag{12}$$

where $(\cdot)^{-T}$ represents the inverse transpose. The Lagrangian strain rate $\dot{\mathbf{E}}^*$ of the lattice can be expressed in terms of $\mathbf{F}^*$ and $\mathbf{D}^*$ as

$$\dot{\mathbf{E}}^* = \mathbf{F}^{*T} \cdot \mathbf{D}^* \cdot \mathbf{F}^*. \tag{13}$$

Equation (12) can be rewritten as

$$\dot{\boldsymbol{\tau}} = \mathscr{L} : \mathbf{D}^* + \boldsymbol{\Omega}^* \cdot \boldsymbol{\tau} - \boldsymbol{\tau} \cdot \boldsymbol{\Omega}^*. \tag{14}$$

The index form of the fourth rank tensor $\mathscr{L}$ in the above equation is derived as

$$\mathscr{L}_{ijkl} = F^*_{ir} F^*_{js} F^*_{kt} F^*_{lu} \mathscr{D}_{rstu} + \tfrac{1}{2}(\delta_{ik}\tau_{jl} + \delta_{il}\tau_{jk} + \tau_{il}\delta_{jk} + \tau_{ik}\delta_{jl}), \tag{15}$$

where δ_{ij} represents the Kronecker delta.

The nominal stress $\mathbf{n}$ referred to the reference (undeformed) configuration can be related to the Kirchhoff stress $\boldsymbol{\tau}$ referred to the current (deformed) configuration with the relation

$$\boldsymbol{\tau} = \mathbf{F} \cdot \mathbf{n}. \tag{16}$$

The nominal stress rate $\dot{\mathbf{n}}$ can then be obtained as

$$\dot{\mathbf{n}} = \mathbf{F}^{-1} \cdot \dot{\boldsymbol{\tau}} + \dot{\mathbf{F}}^{-1} \cdot \boldsymbol{\tau}. \tag{17}$$

Finally, from eqns (5), (6), (14), and (17), the constitutive relation for the nominal stress rate and the conjugate deformation gradient rate can be formulated concisely as

$$\dot{\mathbf{n}} = \mathbf{K} : \dot{\mathbf{F}} - \dot{\mathbf{B}}, \tag{18}$$

where $\mathbf{K}$ and $\dot{\mathbf{B}}$ are determined by following the derivation in Asaro and Needleman (1985).

Plastic deformation due to crystalline slips in metals is inherently strain rate sensitive. It should be noted that the strain rate sensitivity can significantly influence strain localization in sheet metal operations (for example, see Ghosh and Hecker, 1975; Wang and Wenner, 1978). For rate sensitive materials, all slip systems are assumed to be activated when the resolved shear stresses on the corresponding slip planes are not identically zero. Therefore, a lack of uniqueness for determination of the operative slip systems corresponding to an imposed deformation for rate insensitive materials is alleviated with the consideration of strain rate sensitivity (see Pan and Rice, 1983).

A power-law relation is used to relate the resolved shear-stress $\tau^{(\alpha)}$ $(=\mathbf{m}^{*(\alpha)} \cdot \boldsymbol{\tau} \cdot \mathbf{s}^{*(\alpha)})$ to the shear strain rate $\dot{\gamma}^{(\alpha)}$ of the αth slip system by (for example, see Pan and Rice, 1983)

$$\dot{\gamma}^{(\alpha)} = \dot{a}^{(\alpha)} \left(\frac{\tau^{(\alpha)}}{g^{(\alpha)}}\right) \left(\left|\frac{\tau^{(\alpha)}}{g^{(\alpha)}}\right|\right)^{(1/M)-1}, \tag{19}$$

where $\dot{a}^{(\alpha)}$ is the reference strain rate on the αth slip system and M represents the strain rate sensitivity of crystalline slips. The slip system hardness, $g^{(\alpha)}$, is a function of the sum of the

shear strains of all slip systems, γ. For simplicity, the magnitudes of $\dot{a}^{(\alpha)}$ and $g^{(\alpha)}$ are assumed to be the same for all slip systems. The evolution of the slip system hardness is given by

$$\dot{g}^{(\alpha)} = \sum_{\beta} h_{\alpha\beta} |\dot{\gamma}^{(\beta)}|, \tag{20}$$

where $h_{\alpha\beta}$, the components of the hardening matrix **h**, define the relationship between the hardening rate of the αth slip system and that of the βth slip system.

A simple hardening matrix, similar to that adopted in Asaro and Needleman (1985), is adopted here:

$$h_{\alpha\beta} = q_{\alpha\beta} h^{(\beta)}, \tag{21}$$

where $q_{\alpha\beta}$, the components of the matrix **q**, are related to the self hardening rate on the primary slip system and the latent hardening rate on the secondary slip system of a crystal, and $h^{(\beta)}$ is a function of $g^{(\beta)}$, as in Bronkhorst *et al.* (1992)

$$h^{(\beta)} = h_0 \left(1 - \frac{g^{(\beta)}}{g_s^{(\beta)}}\right)^r. \tag{22}$$

Here h_0, r, and $g_s^{(\beta)}$ are the slip system hardening parameters which are assumed to be constant for all slip systems. The saturated slip hardness $g_s^{(\beta)}$ is assumed to be a function of temperature. Nevertheless, the change of $g_s^{(\beta)}$ is not a major consideration at low temperature. All parameters above can be obtained by fitting the stress–strain curve of a uniaxial tensile test.

Low-carbon steels have body centered cubic crystal structures at low homologous temperature. For example, if only the twelve $\{110\}\langle 111\rangle$ slip systems are considered for b.c.c. metals, there are six different slip planes with two slip directions on each plane. Therefore, the matrix **q** defined in eqn (21) can be specified as

$$q = \begin{bmatrix} \mathbf{G} & q_n\mathbf{H} & q_n\mathbf{H} & q_n\mathbf{H} & q_n\mathbf{H} & q_n\mathbf{H} \\ q_n\mathbf{H} & \mathbf{G} & q_n\mathbf{H} & q_n\mathbf{H} & q_n\mathbf{H} & q_n\mathbf{H} \\ q_n\mathbf{H} & q_n\mathbf{H} & \mathbf{G} & q_n\mathbf{H} & q_n\mathbf{H} & q_n\mathbf{H} \\ q_n\mathbf{H} & q_n\mathbf{H} & q_n\mathbf{H} & \mathbf{G} & q_n\mathbf{H} & q_n\mathbf{H} \\ q_n\mathbf{H} & q_n\mathbf{H} & q_n\mathbf{H} & q_n\mathbf{H} & \mathbf{G} & q_n\mathbf{H} \\ q_n\mathbf{H} & q_n\mathbf{H} & q_n\mathbf{H} & q_n\mathbf{H} & q_n\mathbf{H} & \mathbf{G} \end{bmatrix}, \tag{23}$$

with

$$\mathbf{G} = \begin{bmatrix} 1 & q_c \\ q_c & 1 \end{bmatrix} \tag{24}$$

and

$$\mathbf{H} = \begin{bmatrix} 1 & 1 \\ 1 & 1 \end{bmatrix}, \tag{25}$$

where q_c represents the ratio of latent hardening rate to self hardening rate for coplanar slip systems and q_n represents the ratio of latent hardening rate to self hardening rate for noncoplanar slip systems. Here, q_c and q_n are assumed to be constant throughout the deformation history. The value of q_c is approximately 1.2 whereas that of q_n ranges approximately from 1.2 to 1.4 for an iron single crystal (Keh, 1965; Nakada and Keh, 1966). Note

that Taylor's isotropic hardening (Taylor and Elam, 1923) is recovered when the values of q_c and q_n are equal to unity. When the value of q_n is larger than that of q_c, the form of **q** adopted in eqn (23) implies that the hardening rates of the noncoplanar slip systems are larger than those of the coplanar ones.

For the $\{112\}\langle 111\rangle$ slip system, there are twelve different slip planes with one slip direction on each plane. Therefore, **q** in eqn (23) becomes a 12×12 matrix where **G** in eqn (24) and **H** in eqn (25) degenerate to a scalar of unity. Note that since there is only one slip direction on each slip plane, the concept of coplanar latent hardening is no longer applicable. However, noncoplanar latent hardening in terms of q_n is still applicable here.

For the pencil glide system, which is our main interest, we have a total of four slip directions. We search for the slip plane, even a noncrystallographic one, to give the maximum value of the resolved shear stress for a given slip direction. In order to make a tractable simulation for hardening, we assume the Taylor hardening for slips occur for a given $\langle 111\rangle$ direction and the latent hardening constant $q_n = 1.4$ for slips along the other $\langle 111\rangle$ directions.

By using a linear interpolation scheme (for example, see Peirce *et al.*, 1984), the increment of the shear strain of the αth slip system at time t can be expressed as

$$\Delta\gamma^{(\alpha)} = [(1-\theta)\dot{\gamma}^{(\alpha)}(t)+\theta\dot{\gamma}^{(\alpha)}(t+\Delta t)]\Delta t, \tag{26}$$

where θ is an interpolation parameter specified from 0 to 1. Furthermore, since the shear strain rate $\dot{\gamma}^{(\alpha)}$ defined in eqn (19) is a function of the resolved shear stress $\tau^{(\alpha)}$ and the slip system hardness $g^{(\alpha)}$, the shear strain rate at time $t+\Delta t$ can be approximately obtained by using a Taylor series expansion as

$$\dot{\gamma}^{(\alpha)}(t+\Delta t) \simeq \dot{\gamma}^{(\alpha)}(t)+\frac{\partial\dot{\gamma}^{(\alpha)}}{\partial\tau^{(\alpha)}}\Delta\tau^{(\alpha)}+\frac{\partial\dot{\gamma}^{(\alpha)}}{\partial g^{(\alpha)}}\Delta g^{(\alpha)}. \tag{27}$$

As in Peirce *et al.* (1982), the final form of the increment of the shear strain is given by

$$\sum_{\beta} N_{\alpha\beta}\Delta\gamma^{(\beta)} = (\dot{\gamma}^{(\alpha)}(t)+\mathbf{Q}^{(\alpha)}:\mathbf{D})\Delta t, \tag{28}$$

where $N_{\alpha\beta}$ and $\mathbf{Q}^{(\alpha)}$ are listed in Asaro and Needleman (1985).

Once the constitutive behavior of an individual grain is known, the transition from the micro-response of the individual grain to the macro-response of the aggregate follows the averaging scheme developed by Hill (1972).

2.3. *Various slip systems*

For b.c.c. crystals, three possible slip systems, namely, $\langle 111\rangle$ pencil glide, $\{110\}\langle 111\rangle$, and $\{112\}\langle 111\rangle$, are assumed. Based on the concept of the $\langle 111\rangle$ pencil glide, any planes, even non-crystallographic ones, containing $\langle 111\rangle$ slip directions with the maximized resolved shear stress are considered to be the slip planes. Hence, there are four slip planes associated with the $\langle 111\rangle$ pencil glide system. For the $\{110\}\langle 111\rangle$ slip system there are six slip planes with two slip directions on each plane, whereas for the $\{112\}\langle 111\rangle$ slip system, there are twelve slip planes with one slip direction on each plane. Numerical results based on the three slip systems in the polycrystal model are presented in Section 4.

2.4. *Crystallographic texture*

Among several factors inducing plastic anisotropy in metals, such as the orientation, arrangement, and shape of the grains, the orientation of the grains dominates the anisotropic phenomenon up to moderately large strains. Three Euler angles relating the crystal coordinates of each grain to the material coordinates of the aggregate are adopted to represent the crystallographic orientations of each grain. There are three most widely used representations of the Euler angles. We adopt the one with the sequence of rotation of the axes

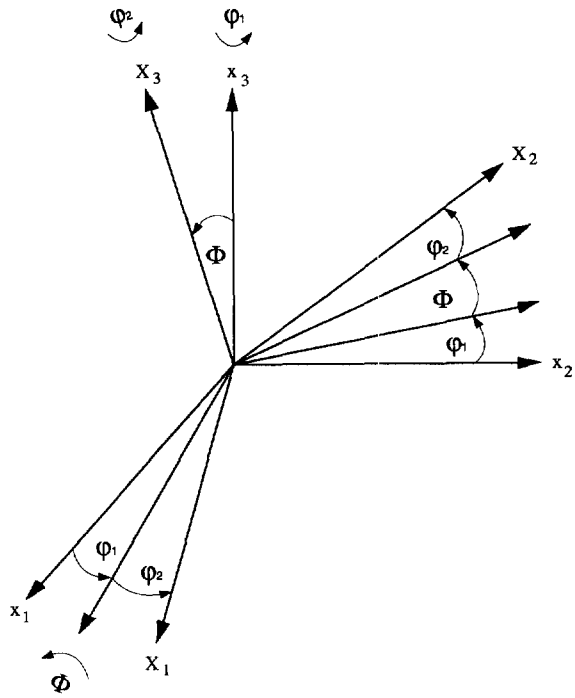

Fig. 2. Representation of the Euler angles.

shown in Fig. 2 where φ_1, Φ and φ_2 are the Euler angles and **X** and **x** represent the crystal (local) coordinates and the material (global) coordinates, respectively. The sequence of rotation is explained in the following.

(1) A rotation of φ_1 angle about the x_3 axis.
(2) A rotation of Φ angle about the rotated x_1 axis.
(3) Finally a rotation of φ_2 angle about the rotated x_3 axis.

Here φ_1 ranges between 0 and 2π, Φ ranges between 0 and π and φ_2 ranges between 0 and 2π. The relationships between the responses of the crystal coordinates and those of the material coordinates can be obtained according to the transformation law

$$\mathbf{x} = \boldsymbol{\Psi} \cdot \mathbf{X}, \tag{29}$$

where the transformation matrix $\boldsymbol{\Psi}$ corresponding to this representation of the Euler angles is defined as

$$\boldsymbol{\Psi} = \begin{bmatrix} \cos\varphi_1 \cos\varphi_2 - \sin\varphi_1 \sin\varphi_2 \cos\Phi & -\cos\varphi_1 \sin\varphi_2 - \sin\varphi_1 \cos\varphi_2 \cos\Phi & \sin\varphi_1 \sin\Phi \\ \sin\varphi_1 \cos\varphi_2 + \cos\varphi_1 \sin\varphi_2 \cos\Phi & -\sin\varphi_1 \sin\varphi_2 + \cos\varphi_1 \cos\varphi_2 \cos\Phi & -\cos\varphi_1 \sin\Phi \\ \sin\varphi_2 \sin\Phi & \cos\varphi_2 \sin\Phi & \cos\Phi \end{bmatrix}. \tag{30}$$

We select a sufficiently large number of grains to simulate uniformly distributed crystal orientations for isotropic materials. The initial Euler angles of each grain are obtained via a random number generator. After imposing arbitrary loading paths on initially isotropic materials, the crystallographic texture of the corresponding pre-strained materials can be simulated by updating the Euler angles of each grain. It is noteworthy that the crystallographic texture can also be characterized by using the crystallographic orientation

distribution function (CODF) (for example, see Bunge, 1982) constructed from X-ray diffraction data.

2.5. *Boundary conditions*

Typically there are two types of boundary conditions for the Taylor-type polycrystal models: all-displacement and displacement-traction (mixed) boundary conditions. As explained in Asaro and Needleman (1985), due to the available rate constitutive relation for the Taylor-like polycrystal model, it is natural to simulate homogeneous boundary value problems based on boundary conditions of both displacement and traction for polycrystals rather than to make assumptions about the unspecified components of the strain rate. In order to benchmark the influences of the selected boundary conditions, the stress–strain response of an isotropic copper (face centered cubic (f.c.c.) metal) under uniaxial tensile loading based on these two boundary conditions is plotted in Fig. 3. In the figure, the stress–strain relation from Bronkhorst *et al.* (1992) based on the all-displacement boundary conditions is also included for comparison. It should be noted that the stress–strain relations based on the all-displacement boundary conditions from Bronkhorst *et al.* (1992) and from the current study are in good agreement although the detailed formulations are slightly different. The stress–strain curve based on the mixed boundary conditions is slightly lower than that based on the all-displacement boundary conditions. In general, the stress–strain relations based on these two boundary conditions are in good agreement as shown.

Implementation of the mixed boundary conditions into the polycrystal model is now elaborated under both plane-strain compressive and proportional in-plane tensile loading conditions. The coordinate system and the geometry of the material are shown in Fig. 4 where $\mathbf{x}_1$, $\mathbf{x}_2$ and $\mathbf{x}_3$ indicate the rolling, transverse and compressive direction, respectively. Plane-strain compression requires that the normal strain rate in the transverse ($\mathbf{x}_2$) direction be equal to zero. Therefore, the deformation gradient $\bar{F}_{22}$ is equal to 1. Here, $(\bar{\ })$ represents the corresponding quantity of the aggregate. The incremental normal strain rate is the

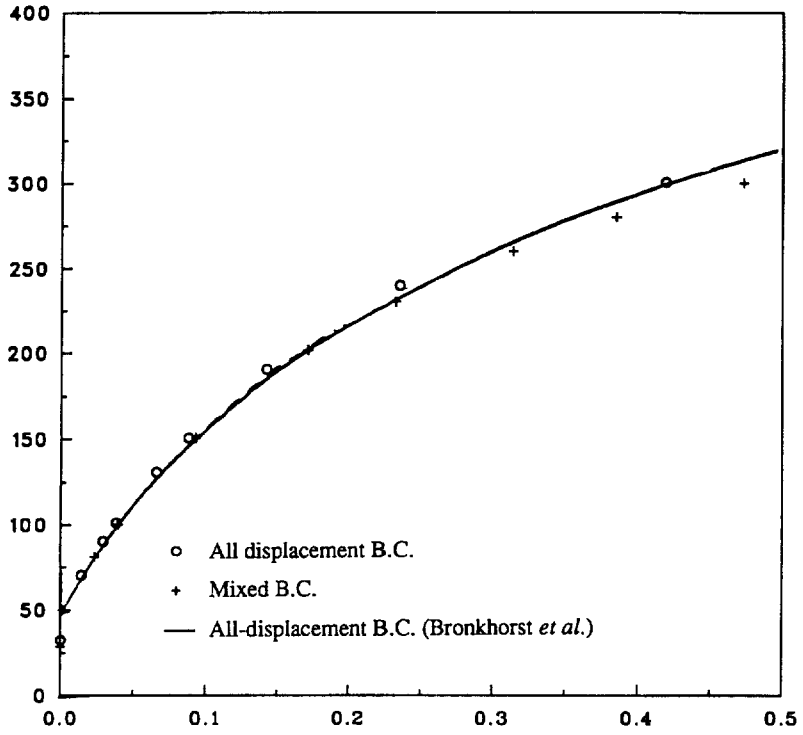

Fig. 3. The uniaxial tensile stress–strain relations from the simulations based on the all-displacement boundary conditions, the displacement-traction boundary conditions and from Bronkhorst *et al.* (1992) for copper.

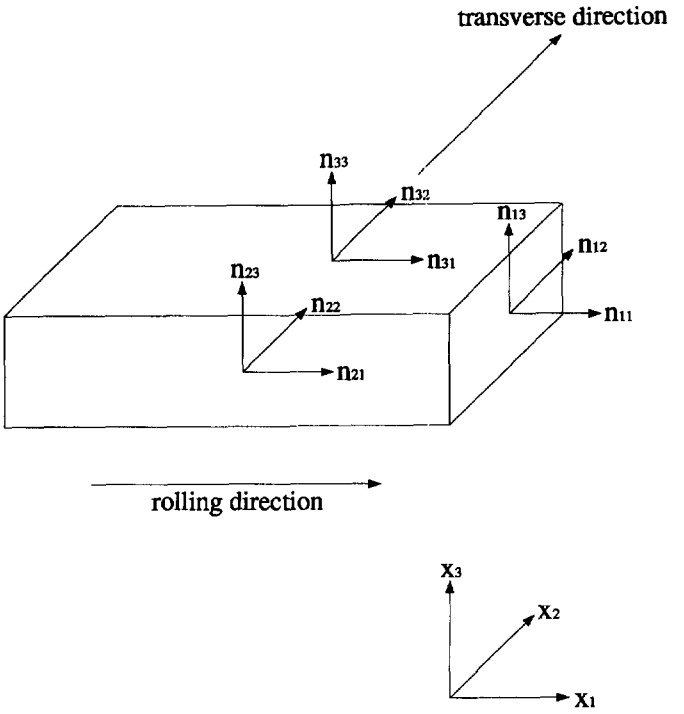

Fig. 4. The coordinate system of the sheet metal.

compressive ($\mathbf{x}_3$) direction is assumed to be prescribed. The hypothesis of the compressive conditions is that lines of the material in the sheet plane ($\mathbf{x}_1$–$\mathbf{x}_2$ plane) remain consistently in that plane and the rigid body rotation about the loading axis is constrained as well. Hence

$$\begin{aligned} \bar{\mathbf{F}} \cdot \mathbf{e}_1 &= \bar{F}_{11}\mathbf{e}_1 \\ \bar{\mathbf{F}} \cdot \mathbf{e}_2 &= \bar{F}_{22}\mathbf{e}_2, \end{aligned} \tag{31}$$

where $\mathbf{e}_1$ and $\mathbf{e}_2$ are the unit vectors in the $\mathbf{x}_1$ and $\mathbf{x}_2$ directions, respectively. Equation (31) leads to

$$\bar{F}_{21} = 0, \quad \bar{F}_{31} = 0, \quad \bar{F}_{12} = 0, \quad \bar{F}_{32} = 0. \tag{32}$$

The nominal stress boundary conditions corresponding to plane-strain compression are

$$\begin{aligned} \bar{n}_{11} &= 0 \quad \text{on } \mathbf{x}_1 = \text{constant} \\ \bar{n}_{31} = \bar{n}_{32} &= 0 \quad \text{on } \mathbf{x}_3 = \text{constant}. \end{aligned} \tag{33}$$

Under the subsequent proportional in-plane biaxial tensile loading, the in-plane ($\mathbf{x}_1$–$\mathbf{x}_2$ plane) stresses are considered to be nonzeros. We assume that the incremental normal strain in the rolling ($\mathbf{x}_1$) direction is prescribed. The nominal stress rate ratios, $\dot{\bar{n}}_{22}/\dot{\bar{n}}_{11}$ and $\dot{\bar{n}}_{12}/\dot{\bar{n}}_{11}$, are taken as constants. The remaining boundary conditions are

$$\dot{\bar{F}}_{12} = \dot{\bar{F}}_{21}, \quad \dot{\bar{F}}_{31} = 0, \quad \dot{\bar{F}}_{32} = 0 \tag{34}$$

$$\dot{\bar{n}}_{31} = 0, \quad \dot{\bar{n}}_{32} = 0, \quad \dot{\bar{n}}_{33} = 0. \tag{35}$$

2.6. *Material properties*

For iron single crystals, three cubic elastic constants in eqn (10) can be found in the handbook (*Smithells Metals Reference Book*, 1983) as

$$C_{11} = 237 \text{ GPa}$$
$$C_{12} = 141 \text{ GPa}$$
$$C_{44} = 116 \text{ GPa}. \tag{36}$$

The microscopic strain rate sensitivity M for single crystals in eqn (19) is assumed to be 0.012 which is the macroscopic strain rate sensitivity of the aggregates (Ghosh and Hecker, 1975). The values of q_c and q_n in eqn (23) are set to 1.2 and 1.4 (Nakada and Keh, 1966), respectively.

A parallel experimental investigation of the texture of low-carbon hot-rolled steels was conducted by Friedman *et al.* (1997). In this study, uniaxial tensile data were collected up to a maximum tensile strain of approximately 0.25. The power-law relation $\bar{\sigma} = 647.9(\bar{\varepsilon})^{0.197}$ is used to fit the experimental data. The power-law relation is then used to guide the stress–strain behavior at large strains. The experimental stress–strain curve and the power-law fit are shown in Fig. 5. It should be noted that the Lüders strain exhibited in the test cannot be fitted well by the power-law stress–strain relation.

Since we anticipate large plastic strain under plane-strain compressive loading and the subsequent in-plane loading, the stress–strain relation based on the polycrystal model is fitted to the uniaxial tensile power-law relation at large strains by adjusting the slip hardening parameters h_0, r, and $g_s^{(\beta)}$ as well as the initial values of $g_0^{(\alpha)}$ in the polycrystal model. After trial-and-error, the simulated stress–strain curve for 400 randomly oriented grains based on the $\langle 111 \rangle$ pencil glide system is shown in Fig. 5 and the corresponding parameters are tabulated in Table 1. The parameters for the simulated stress–strain curve based on the other two slip systems are also listed in Table 1. Note that the magnitudes of these constants cannot be uniquely determined since there are four adjustable parameters in eqn (22).

Note that the effects of the number of grains for the polycrystal model on the uniaxial tensile stress–strain relations are shown in Fig. 6. The results of the simulations indicate that the stress–strain curve based on 400 grains nearly coincides with that based on 800 grains. Therefore, 400 grains are used in our simulations for plane-strain compression and the subsequent in-plane biaxial loading to save computational time.

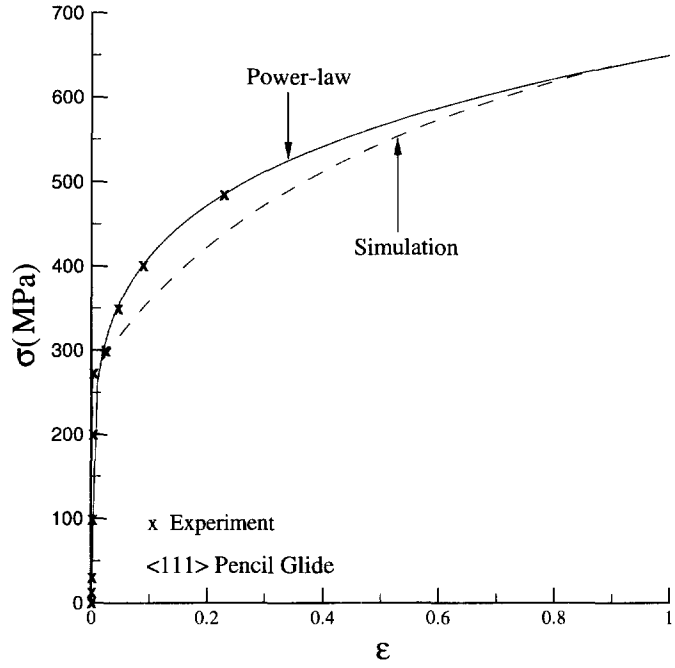

Fig. 5. The uniaxial tensile stress–strain relations from the experiment and from the simulations based on the $\langle 111 \rangle$ pencil glide system for a low-carbon steel. The fitted power-law relation is also shown.

Table 1. The hardening parameters used to fit the uniaxial tensile stress–strain relation based on the ⟨111⟩ pencil glide, {110} ⟨111⟩, and {112} ⟨111⟩ slip systems

	h_0 (MPa)	$g_s^{(\beta)}$ (MPa)	r	$g_0^{(\alpha)}$ (MPa)
⟨111⟩ pencil glide	350	450	4.30	100
{110} ⟨111⟩	330	365	4.15	100
{112} ⟨111⟩	330	395	4.15	100

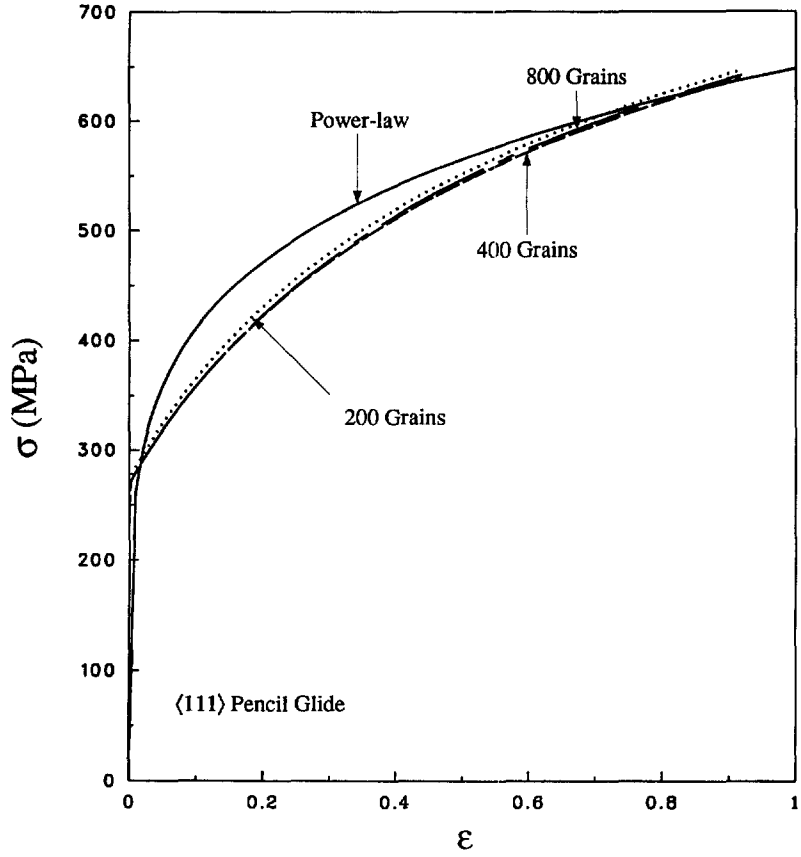

Fig. 6. The uniaxial tensile stress–strain relations from the simulations based on randomly oriented 200, 400, and 800 grains for the low-carbon steel.

3. COMPUTATIONAL PROCEDURE

Sheet rolling processes of an initially isotropic material are simulated with plane-strain compression. Pole figures are used to represent the crystallographic textures of the sheet metal at various compressive thickness strains after unloading. The yield surfaces of the compressed sheet metal are then determined under the subsequent proportional in-plane loading. Our computational procedures are summarized as follows.

The deformation gradient $\bar{\mathbf{F}}$ of the aggregate should be a second order identity tensor before imposing any deformation on the initially isotropic aggregate. The isotropic aggregate consists of many (400) randomly oriented grains. When Taylor's assumption is adopted, the deformation gradient of each grain (single crystal) is the same as that of the aggregate. For each grain, three Euler angles, φ_1, Φ, and φ_2, as well as the corresponding transformation matrix $\boldsymbol{\Psi}$ defined in eqn (30) can be obtained. The elastic modulus $\mathscr{D}$, the slip direction vector $\mathbf{s}^{(\alpha)}$ and the slip plane normal vector $\mathbf{m}^{(\alpha)}$ of the αth slip system of each grain based on the crystal coordinates (the local coordinates) are transformed to the

corresponding quantities based on the material coordinates (the global coordinates) by using the transformation relation as

$$(\mathscr{D}_{ijkl})_{\text{global}} = \Psi_{ir}\Psi_{js}\Psi_{kt}\Psi_{lu}(\mathscr{D}_{rstu})_{\text{local}} \tag{37}$$

$$(\mathbf{s}^{(\alpha)})_{\text{global}} = \boldsymbol{\Psi}\cdot(\mathbf{s}^{(\alpha)})_{\text{local}} \tag{38}$$

$$(\mathbf{m}^{(\alpha)})_{\text{global}} = \boldsymbol{\Psi}\cdot(\mathbf{m}^{(\alpha)})_{\text{local}}. \tag{39}$$

Here $(\cdot)_{\text{global}}$ and $(\cdot)_{\text{local}}$ represent the corresponding quantities based on the global coordinates and local coordinates, respectively. The matrices $\mathbf{K}$ and $\dot{\mathbf{B}}$ of each grain defined in eqn (18) and the shear strain rate of the αth slip system, $\dot{\gamma}^{(\alpha)}$, defined in eqn (19) can then be obtained. All the calculations above are applied to each grain.

Hill's averaging theorem is followed with the assumptions of uniform deformation throughout the aggregate and the same volume fraction for each grain. The $\bar{\mathbf{K}}$ and $\dot{\bar{\mathbf{B}}}$ of the aggregate can be obtained using a simple arithmetic averaging scheme for the corresponding quantities of grains

$$\bar{\mathbf{K}} = \frac{1}{\text{Num}}\sum_{c=1}^{\text{Num}}\mathbf{K} \tag{40}$$

$$\dot{\bar{\mathbf{B}}} = \frac{1}{\text{Num}}\sum_{c=1}^{\text{Num}}\dot{\mathbf{B}}. \tag{41}$$

Here, "Num" represents the total number of grains. The rate of deformation gradient of aggregate, $\dot{\bar{\mathbf{F}}}$, and the rate of deformation of the aggregate, $\bar{\mathbf{D}}$, at the current time t under plane-strain compression can be obtained based on the mixed boundary conditions as described early. The increment of the shear strain, $\Delta\gamma^{(\alpha)}$, and the increment of the slip hardness of the αth slip system, $\Delta g^{(\alpha)}$, are obtained via eqns (28) and (20), respectively. The magnitudes of $\gamma^{(\alpha)}$, $g^{(\alpha)}$, $\mathbf{K}$, and $\dot{\mathbf{B}}$ of each grain at time $t+\Delta t$ for the next increment of strain can also be evaluated. The plastic part of the deformation gradient, $\mathbf{F}^p$, at time $t+\Delta t$ can be obtained from the relation $\dot{\mathbf{F}}^p\cdot(\mathbf{F}^p)^{-1} = \Sigma_\alpha\dot{\gamma}^{(\alpha)}\mathbf{s}^{(\alpha)}\mathbf{m}^{(\alpha)}$. The deformation gradient $\mathbf{F}^*$ of a single crystal based on the lattice at time $t+\Delta t$ can then be calculated by

$$\mathbf{F}^* = \mathbf{F}\cdot(\mathbf{F}^p)^{-1}. \tag{42}$$

The nominal stress rate $\dot{\mathbf{n}}$ of each grain can be obtained by using eqn (18). The nominal stress rate of the aggregate, $\dot{\bar{\mathbf{n}}}$, is obtained by using a simple arithmetic averaging scheme for the nominal stress rates of each grain, $\dot{\mathbf{u}}$, as

$$\dot{\bar{\mathbf{n}}} = \frac{1}{\text{Num}}\sum_{c=1}^{\text{Num}}\dot{\mathbf{n}}. \tag{43}$$

Finally, the nominal stress of the aggregate, $\bar{\mathbf{n}}$, at time $t+\Delta t$ can be obtained corresponding to the prescribed mixed boundary conditions.

Under the subsequent proportional in-plane loading, the boundary conditions need to be changed and the transformation matrix $\boldsymbol{\Psi}$, the slip systems $(\mathbf{s}^{*(\alpha)}, \mathbf{m}^{*(\alpha)})$, and the slip hardness $g^{(\alpha)}$ need to be employed as the initial values for each grain after the elastic unloading of the plane-strain compression.

4. NUMERICAL RESULTS

4.1. *Plane-strain compressive tests*

Plane-strain compressive tests were performed by Friedman *et al.* (1997) on a low-carbon hot-rolled steel sheet to simulate cold rolling. The mechanical behavior of the steel and the details of the experiments can be found in Friedman *et al.* (1997). The compressive stresses, with and without friction correction (for example, see Hosford and Caddell, 1993), as functions of the compressive thickness strains obtained from the experiments are shown in Fig. 7. The compressive stress–strain relations from the simulations, based on the three chosen slip systems, are also shown in Fig. 7. The stress–strain relation based on the $\{110\}\langle 111\rangle$ slip system approaches the experimental results without friction force correction. However, the simulated stress–strain relations based on the $\langle 111\rangle$ pencil glide system and the $\{112\}\langle 111\rangle$ slip system are in good agreement with the experimental results corrected for friction.

The reason that the $\langle 111\rangle$ pencil glide system gives the lowest stress–strain relation is possibly due to an increase in freedom for the selection of the slip system. It should be noted that the material parameters for the different slip systems are obtained by fitting the uniaxial power-law stress–strain relation at large strains. The differences of the simulated uniaxial stress–strain relations will carry over to the plane-strain compressive stress–strain relations. However, the good agreement of the results from the simulations and the experiments shown in Fig. 7 could be regarded as one validation of the present polycrystal model.

4.2. *Pole figures of texture sheet metal*

The textures of the b.c.c. sheet metal at various compressive thickness strains of 0 (initially isotropic), 0.34 and 0.79, in terms of (200) and (110) pole figures, based on the

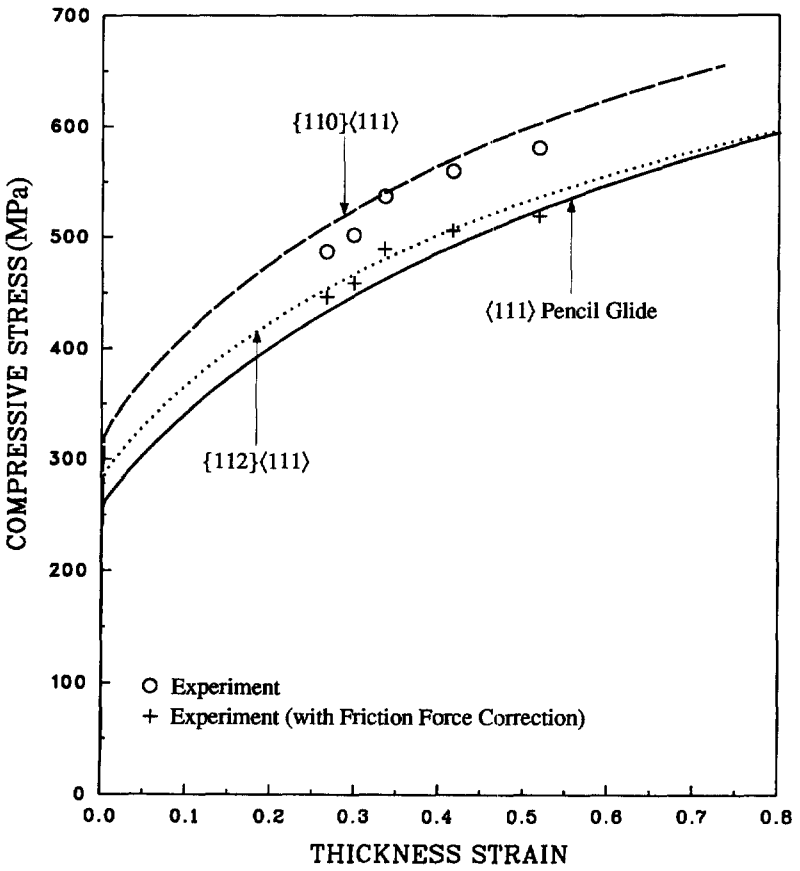

Fig. 7. The plane-strain compressive stress–strain relations from the experiment and from the simulations based on the $\langle 111\rangle$ pencil glide, $\{110\}\langle 111\rangle$, and $\{112\}\langle 111\rangle$ slip system for a low-carbon steel.

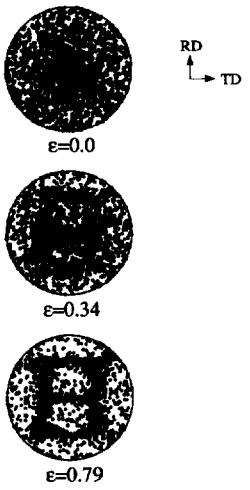

(200) Pole Figure

Fig. 8. The (200) pole figures obtained from the simulations based on the ⟨111⟩ pencil glide system after plane-strain compression with the compressive thickness strain of 0.0 (isotropic), 0.34 and 0.79.

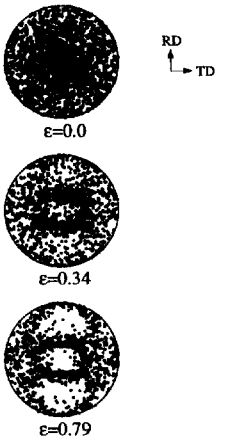

(110) Pole Figure

Fig. 9. The (110) pole figures obtained from the simulations based on the ⟨111⟩ pencil glide system after plane-strain compression with the compressive thickness strain of 0.0 (isotropic), 0.34 and 0.79.

⟨111⟩ pencil glide system are shown in Figs 8 and 9 where "RD" and "TD" represent the rolling and transverse directions, respectively. It should be noted that, in general, as-received sheet metals contain some degree of plastic anisotropy. However, the slight degree of anisotropy found in the as-received material in the study of Friedman *et al.* (1997) was insignificant when compared with the anisotropy induced from the plane-strain compression at large strains. However, in our simulations, no preferred orientation of grains is assumed before plane-strain compression.

The top figure of Fig. 8 shows no preferred orientation of grains before plane-strain compression. The middle figure of Fig. 8 shows that (200) pole figure exhibits a distinct pattern after plane-strain compression with the compressive thickness strain of 0.34. The bottom figure of Fig. 8 shows a sharp crystallographic texture after plane-strain compression with the compressive thickness strain of 0.79. Figure 8 shows that the (200) planes of grains tend to be parallel to the transverse direction of the rolled sheet at certain preferred angles.

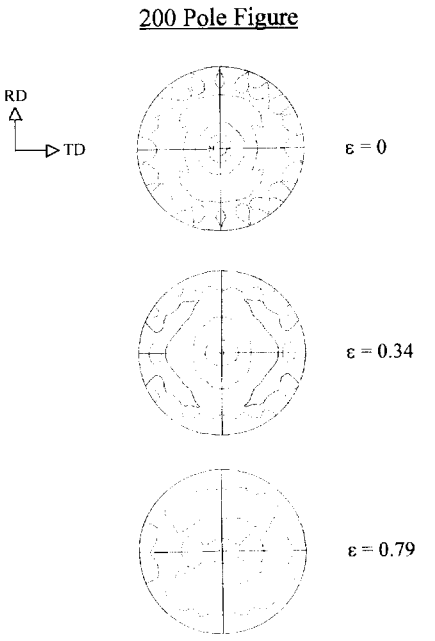

Fig. 10. The (200) pole figure obtained from the experiment after plane strain compression with the compressive thickness strains of 0, 0.34 and 0.79.

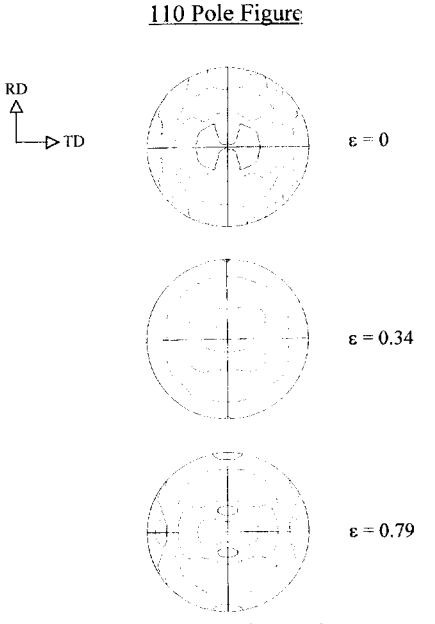

Fig. 11. The (110) pole figure obtained from the experiment after plane strain compression with the compressive thickness strains of 0, 0.34 and 0.79.

Figure 9 shows the texture development in terms of (110) pole figures. The crystallographic textures are symmetric with respect to the RD and TD as shown in both Figs 8 and 9.

Experimental (200) and (110) pole figures (contour plots) provided by Friedman *et al.* (1997) are shown in Figs 10 and 11, respectively, for the as-received material and the material after being deformed in plane-strain compression to the compressive strains of 0.34 and 0.79. The pole figures were constructed by using the crystallographic orientation distribution function (CODF). For both the (200) and (110) pole figures, shown in Figs 10 and 11, there are some initial textures at $\varepsilon = 0$ as shown. For the (200) pole figure at

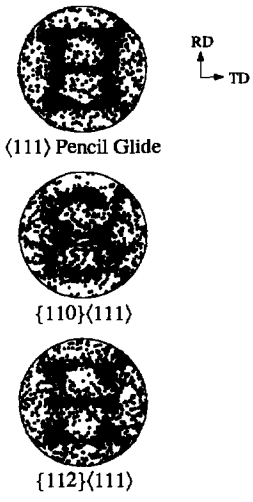

Fig. 12. The (200) pole figures obtained from the simulations based on the ⟨111⟩ pencil glide, {110} ⟨111⟩, and {112} ⟨111⟩ slip systems after plane-strain compression with the compressive thickness strain of 0.79.

$\varepsilon = 0.34$, shown in Fig. 10, the texture is not quite the same as that from the polycrystal model shown in Fig. 8. However, the (200) pole figure at the larger strain of $\varepsilon = 0.79$, shown in Figure 10, agrees well with that in Fig. 8. As shown in Fig. 11, the (110) pole figures at $\varepsilon = 0.34$ and 0.79 agree well with those in Fig. 9. These experimental pole figures indicate that the texture due to the plane-strain compression becomes dominant at large strains and tends to agree with those obtained from the polycrystal model. Note that there are some available experimental pole figures for b.c.c. metals (for example, see Segmüller and Wassermann, 1960). These pole figures in Segmüller and Wassermann (1960) show similar characteristics to those from our simulations.

The (200) and (110) pole figures from our simulations for plane-strain compression with the compressive thickness strain of 0.79 based on the three chosen slip systems are plotted in Figs 12 and 13, respectively. Figure 12 shows a similar pronounced crystallographic texture based on the three slip systems in terms of the (200) pole figures. Figure 13 also shows a similar crystallographic texture based on the three slip systems in terms of the (110) pole figures. From these pole figures, it is difficult to determine the governing slip system in the test.

4.3. *Macroscopic yield surfaces*

As reported by many investigators (for example, see Hecker, 1976), the definition of the initial yield stress significantly affects the shape and size of the initial yield surface and the subsequent yield surface. Several definitions are schematically illustrated in Fig. 14. The proportional limit, denoted as a point 1 in the figure, is a natural and straightforward way to determine the initial yield stress since the permanent deformation starts to occur at this point. Nevertheless, it is not easy to determine the proportional limit point exactly from the measurement. Generally speaking, the stress at 0.2% offset plastic strain (point 2) is usually used as the offset yield stress under uniaxial tensile loading. Many researchers prefer a small but finite (5 to 10 μ) plastic strain (point 3) or use back extrapolation at a given plastic strain (point 4) to determine the initial yield stress under multiaxial loading conditions (for example, see Hecker, 1976). Under multiaxial loading conditions, the effective stress–strain relations under various loading conditions are required for adopting the definitions reviewed above when the usual framework of plasticity theory is followed. However, the effective strain definition is not available unless the effective stress based on the yield function is available.

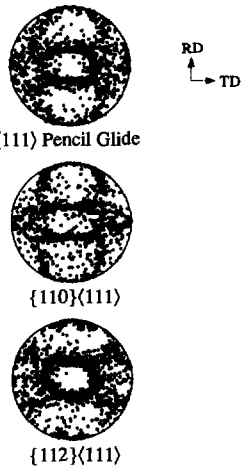

Fig. 13. The (110) pole figures obtained from the simulations based on the ⟨111⟩ pencil glide, {110} ⟨111⟩, and {112} ⟨111⟩ slip systems after plane-strain compression with the compressive thickness strain of 0.79.

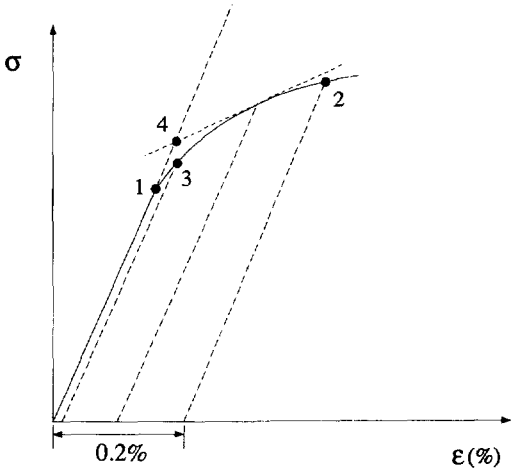

Fig. 14. Representation of various methods to determine the yield stress.

In this work we determine the yield surfaces for sheet metals subjected to proportional in-plane loading after plane-strain compression. The yield surface obtained here is based on the hypotheses of the equivalence of the plastic potential and the yield function with normality flow. Dillamore *et al.* (1971) defined the yield surface by plotting successive surfaces at various levels of plastic work and back extrapolating to zero plastic work. In our study, the yield stress under uniaxial tensile loading in the rolling direction is first determined at 0.02% (definition I hereafter) or 0.2% (definition II hereafter) offset plastic strain. The corresponding plastic work can be obtained with the polycrystal model. The yield surface under proportional in-plane loading is then determined at the plastic work equal to that at 0.02 or 0.2% offset plastic strain in the rolling direction. In this study, we concentrate on the yield behavior in the first quadrant of the in-plane normal stress plane, where both the in-plane normal stresses are positive. The macroscopic yield surfaces from the simulations for both initially isotropic materials and materials after plane-strain compression are investigated here.

Four available phenomenological yield criteria, which account for the planar anisotropy of materials, are fitted to the results of the simulations. In 1948, Hill proposed a quadratic yield criterion (Hill, 1948) for orthotropic materials. This yield criterion has been widely adopted in spite of its failure to encompass the anomalous behavior of some metals. When the out-of-plane shear terms are neglected, the Hill quadratic yield criterion is expressed as

$$F(\sigma_{22}-\sigma_{33})^2+G(\sigma_{33}-\sigma_{11})^2+H(\sigma_{11}-\sigma_{22})^2+2N\sigma_{12}^2=\bar{\sigma}^2, \tag{44}$$

where the coordinate system follows that shown in Fig. 4. Here, $\bar{\sigma}$ represents the effective tensile stress and is considered to be the yield stress under uniaxial tensile loading in the rolling direction. The material constants, F, G, H and N can be determined based on the uniaxial yield stresses in the rolling and transverse directions, the yield stress in the equal biaxial tension direction, and the yield stress under in-plane pure shear.

Based on an upper-bound analysis assuming the $\langle 111\rangle$ pencil glide for rigid-plastic polycrystals, Hosford suggested a yield criterion (Hosford, 1979; Logan and Hosford, 1980) with the requirement that the principal stress directions coincide with the orthotropic directions as

$$F|\sigma_{22}-\sigma_{33}|^m+G|\sigma_{33}-\sigma_{11}|^m+H|\sigma_{11}-\sigma_{22}|^m=\bar{\sigma}^m, \tag{45}$$

where the coordinate system follows that shown in Fig. 4 and $\bar{\sigma}$ is the effective tensile stress defined previously. The constants F, G and H in the equation can be determined from the uniaxial yield stresses in the rolling and transverse directions, and the yield stress in equal biaxial tension direction. After examining several mixed rotationally symmetric textures, Logan and Hosford (1980) recommended the exponent m equal to 6 for b.c.c. and 8 for f.c.c. metals.

Hill (1993) added a pair of cubic terms to his quadratic yield criterion (Hill, 1948) to give the exact values of R in the rolling and transverse directions as specified by the experiments. This yield criterion is written as

$$\frac{\sigma_{11}^2}{\sigma_0^2}-\frac{c\sigma_{11}\sigma_{22}}{\sigma_0\sigma_{90}}+\frac{\sigma_{22}^2}{\sigma_{90}^2}+\left\{(p+q)-\frac{(p\sigma_{11}+q\sigma_{22})}{\sigma_b}\right\}\frac{\sigma_{11}\sigma_{22}}{\sigma_0\sigma_{90}}=1, \tag{46}$$

where the coordinate system follows that shown in Fig. 4. Here σ_0 and σ_{90} represent the uniaxial tensile yield stresses in the rolling and transverse directions, respectively, and σ_b represents the equal biaxial tensile yield stress. Three constants c, p and q can be obtained from the uniaxial yield stresses and the anisotropy parameters in the rolling and transverse directions as well as the yield stress in the equal biaxial tension direction.

Finally, Barlat *et al.* (1997b) proposed a generalized yield criterion, referred to as the Yld96 yield criterion. The yield function cannot be expressed in a simple functional form as those of the three yield criteria discussed above. Therefore we will not repeat the entire formulation of Barlat *et al.* (1997b) here. The yield function follows a long list of works from Hershey (1954), Hosford (1972), Karafillis and Boyce (1993) and Barlat *et al.* (1997a).

4.3.1. $\langle 111\rangle$ *pencil glide system* Figure 15(a) shows the results of the simulated yield surface based on the $\langle 111\rangle$ pencil glide system and definition I for isotropic low-carbon steels. For comparison, the corresponding Tresca yield criterion, the von Mises yield criterion, and the Hosford yield criterion with $m=6$ are also plotted in Fig. 15(a). In the figure, σ_{11} represents the stress in the rolling direction and σ_{22} represents the stress in the transverse direction. The symmetry of the simulated yield surface with respect to equal biaxial direction is shown whereas the yield stresses in the $\mathbf{x}_1$ and $\mathbf{x}_2$ directions are almost the same. The simulated yield surface lies between the Mises and Tresca yield criteria. Note that the simulation results obtained in this study are upper-bound solutions. The simulated yield surface is in good agreement with the yield surface of Hosford with a high exponent

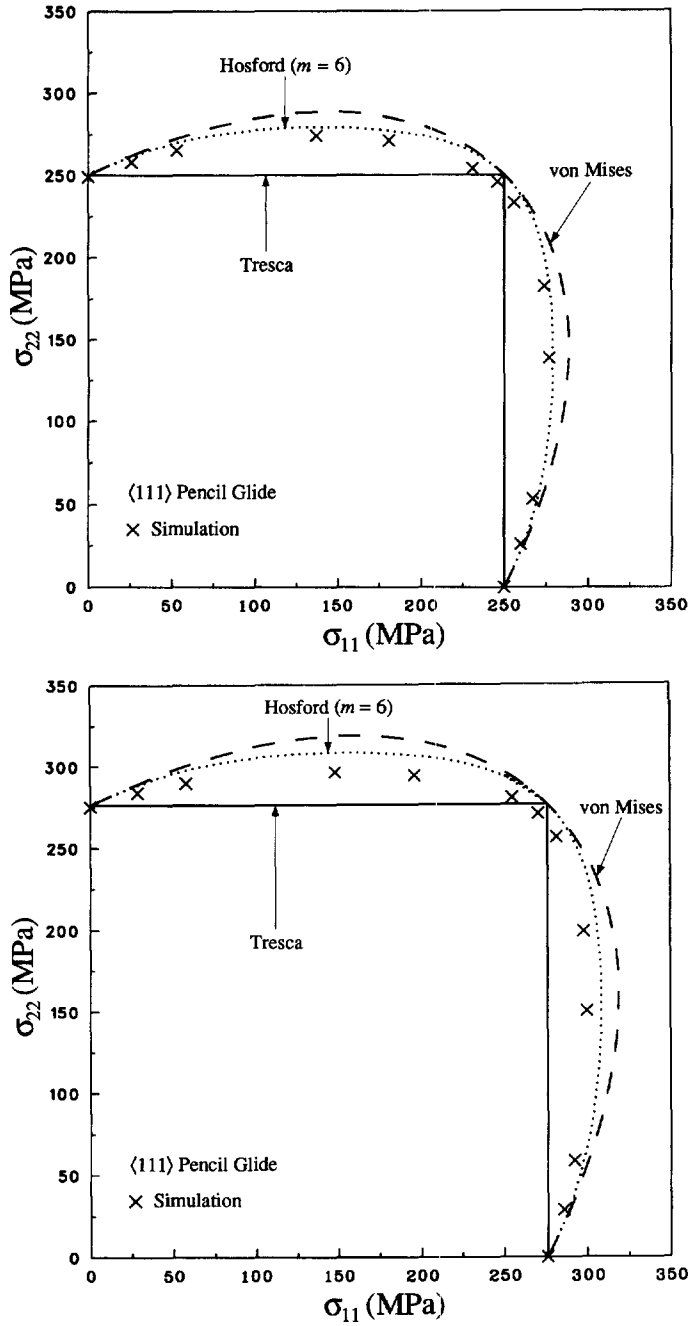

Fig. 15. The results of the simulated yield surface based on the ⟨111⟩ pencil glide system and (a) definition I, (b) definition II and (c) definition I and II (normalized yield surface) compared with those based on the Tresca yield criterion, and von Mises yield criterion, and the Hosford yield criterion with $m = 6$ for isotropic sheets.

of $m = 6$. The simulated yield surface appears to be smooth near the equal biaxial tension direction in contrast to the vertex of the Tresca yield surface.

Figure 15(b) shows the results of the simulated yield surface based on the ⟨111⟩ pencil glide system and definition II for isotropic low-carbon steels. Figure 15(c) shows the results of the simulated yield surfaces based on the ⟨111⟩ pencil glide system and definition I and definition II normalized by the yield stress in the rolling direction. Figure 15(c) indicates that the yield surfaces slightly depend on the amount of plastic work for the initially isotropic steel sheets. Also, the shape of yield surface based on definition II is slightly flatter

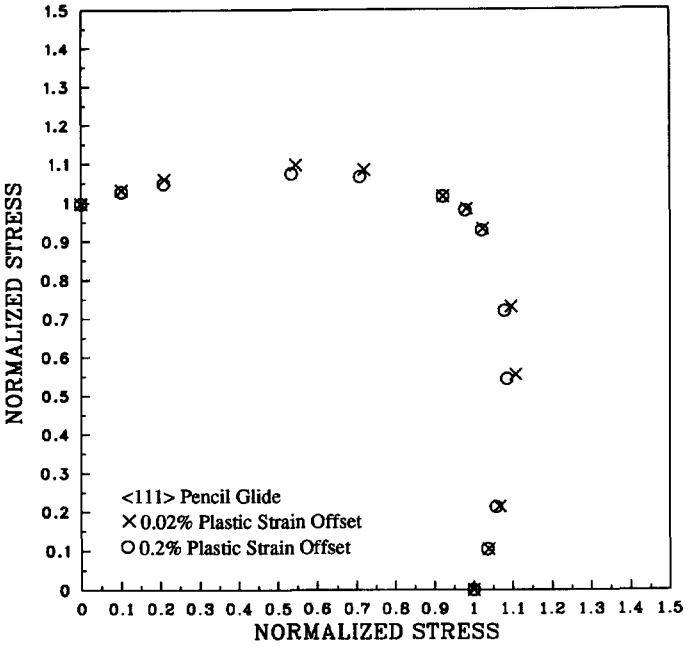

Fig. 15.—*Continued.*

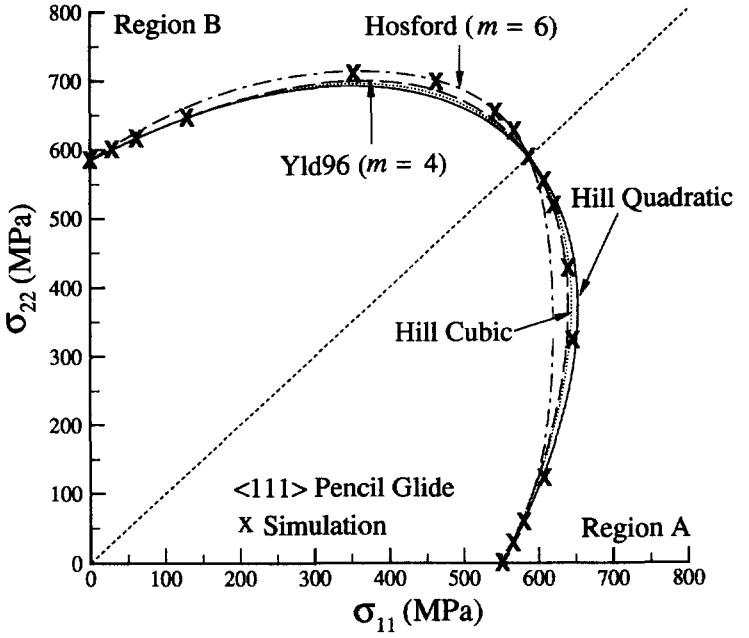

Fig. 16. The results of the simulated yield surface based on the ⟨111⟩ pencil glide system and definition I compared with those on the Hill quadratic and cubic yield criteria, the Hosford yield criterion with $m = 6$, and the Yld96 yield criterion with $m = 4$ for sheets after plane-strain compression with the compressive thickness strain of 0.79.

than that based on definition I in the region between the equal biaxial tension and the uniaxial tension.

Figure 16 shows the results of the simulated yield surface based on the ⟨111⟩ pencil glide system and definition I for steel sheets after plane-strain compression with the compressive thickness strain of 0.79. Note that the directions of the applied in-plane normal stresses coincide with the in-plane orthotropic directions after plane-strain compression.

For convenience of presentation, the region between the equal biaxial tension and the uniaxial tension in the rolling direction is designated as Region A whereas the region between the equal biaxial tension and the uniaxial tension in the transverse direction as Region B. The asymmetry of the yield surface with respect to equal biaxial tension direction indicates the planar anisotropy of the sheet metal. The uniaxial yield stress in the rolling direction is 552 MPa whereas the uniaxial yield stress in the transverse direction is 584 MPa. Both the yield stresses are much higher than the yield stress of 250 MPa before plane-strain compression due to strain hardening. The characteristic of anisotropy will be investigated later by calculating the uniaxial yield stresses, the values of R, and the elastic moduli at various in-plane orientations.

The yield surfaces based on the four available yield criteria fitted to those based on the simulations are shown in Fig. 16. The uniaxial yield stresses in the rolling and transverse directions, and the yield stress under equal biaxial loading from the simulations are used to obtain the constants of the Hill quadratic and Hosford yield functions. Note that we take $m = 6$ for the Hosford yield function following the suggestion of Logan and Hosford (1980) for b.c.c. metals. The uniaxial yield stresses and the values of R in the rolling and transverse directions as well as the yield stress under equal biaxial tension from the simulations are used to determine the constants in the Hill cubic yield criterion. The yield stresses and the R values in the rolling direction, the transverse direction and the direction at 45° from the rolling direction as well as the yield stress under equal biaxial tension conditions from the simulations are used to determine the Yld96 yield function of Barlat *et al.* (1997b).

As shown in Fig. 16, near the uniaxial tension in the rolling and transverse directions, the simulation results agree with the Hill quadratic and cubic yield criteria. In Region A near equal biaxial loading, the simulation results agree with the Hill quadratic, Hill cubic and Yld96 yield criteria whereas in Region B near equal biaxial loading, the simulation results agree with the Hosford yield criterion. The exponent of the Yld96 yield criterion is chosen as 4, instead of the value of 6, suggested by Logan and Hosford (1980) for b.c.c. metals. In passing, the shear yield stresses σ_{xy}, σ_{yz} and σ_{zx} are 293, 295 and 324 MPa, respectively. These values can be used as references in general three-dimensional finite element simulations of sheet forming processes when both the in-plane and out-of-plane shear stresses are considered.

Figure 17 shows the results of the simulated yield surface based on the $\langle 111 \rangle$ pencil glide system and definition II. The yield surfaces based on the above mentioned four yield criteria are also shown. As shown in the figure, the simulation results agree with the Hosford, Hill cubic and Yld96 yield criteria in Region A, whereas the simulation results agree with the Hill quadratic yield criterion in Region B.

The simulated yield surfaces based on definition I and II are redrawn in Fig. 18 for comparison. The slopes of the yield surfaces for a given stress ratio based on definition I and II are quite different near the rolling direction. This implies that there are potentially large differences of the values of R based on these two definitions near the rolling direction. Theoretically speaking, since the initial yield surface should be defined as the one when the plastic dissipation approaches to zero for computational applications to determine the initial small amount of plastic flow, the yield surface based on the offset plastic strain of 0.02% (definition I) is adopted for the rest of the paper.

A shear stress with respect to the rolling and transverse directions occurs when the principal stress directions do not coincide with the symmetry axes of orthotropy. The simulated yield surfaces for constant ratios of the shear stress to the yield stress in the rolling direction, $\sigma_{12}\bar{\sigma}(\equiv s)$, of 0.2, 0.3, and 0.4, projected on the in-plane normal stress plane, are obtained and plotted in Fig. 19(a). Here $\bar{\sigma}$ represents the effective tensile stress defined previously. Figure 19(b) shows these stresses normalized by the yield stress in the rolling direction. Figure 19(b) shows the similarities of the shapes of the yield surfaces for various shear stress ratios. This indicates that phenomenological yield criteria may be used to take account for the effects of in-plane shear stresses for b.c.c. sheet metals with the $\langle 111 \rangle$ pencil glide system.

The normality of the yield surface at the given amount of plastic work is also checked here. We define the angle α for the slope of the yield surface as

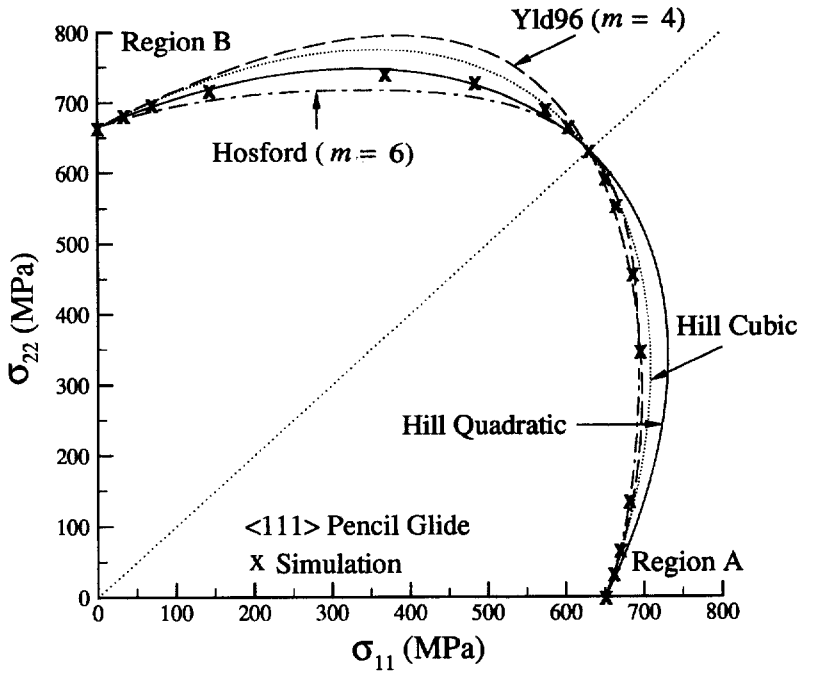

Fig. 17. The results of the simulated yield surface based on the ⟨111⟩ pencil glide system and definition II compared with those on the Hill quadratic and cubic yield criteria, the Hosford yield criterion with $m = 6$, and the Yld96 yield criterion with $m = 4$ for sheets after plane-strain compression with the compressive thickness strain of 0.79.

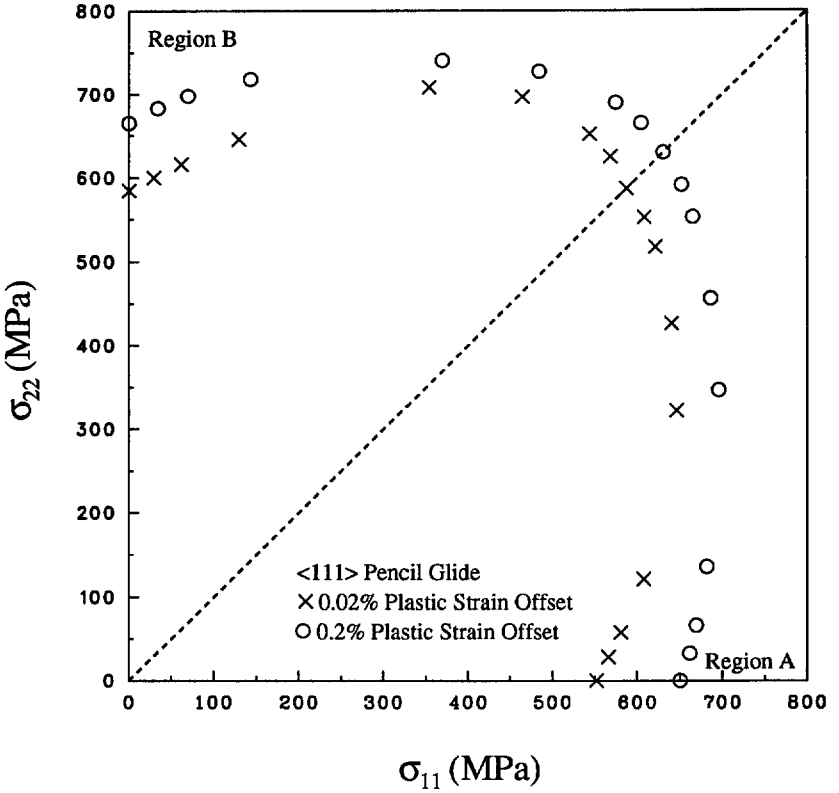

Fig. 18. The results of the simulated yield surfaces based on the ⟨111⟩ pencil glide system and definition I and II for sheets after plane-strain compression with the compressive thickness strain of 0.79.

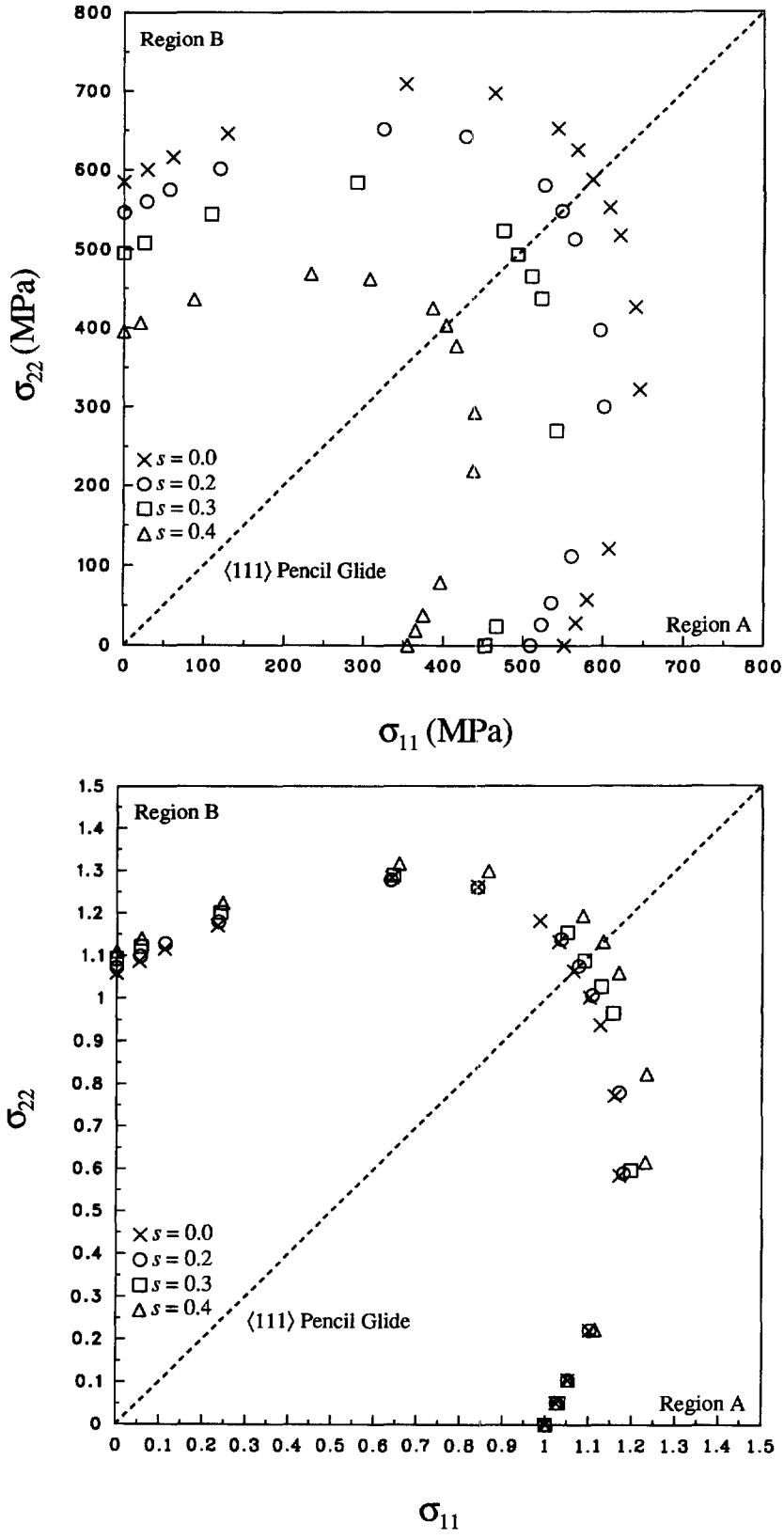

Fig. 19. (a) The results of the simulated yield surfaces and (b) the results of the simulated yield surfaces normalized by the yield stresses in the rolling direction with the shear stress ratio ($\sigma_{12}/\bar{\sigma} \equiv s$) of 0.2, 0.3, and 0.4 based on the ⟨111⟩ pencil glide system and definition I for sheets after plane-strain compression with the compressive thickness strain of 0.79.

$$-\frac{d\sigma_{11}}{d\sigma_{22}} = \tan\alpha. \tag{47}$$

Also we define the plastic flow direction as

$$\frac{d\varepsilon^p_{22}}{d\varepsilon^p_{11}} = \tan\beta. \tag{48}$$

When the normality flow rule is justified as shown in Fig. 20, then

$$-\frac{d\sigma_{11}}{d\sigma_{22}} = \frac{d\varepsilon^p_{22}}{d\varepsilon^p_{11}}, \tag{49}$$

or

$$\alpha = \beta. \tag{50}$$

The values of α and β, defined in Fig. 20 at various ratios of biaxial tension, are tabulated in Table 2. Table 2 indicates that the direction of the increment of the plastic strain is approximately perpendicular to the yield surface at the corresponding yield locus. The normality flow rule is approximately satisfied at the given amount of plastic work based on the polycrystal model.

Figures 21(a)–(c) show the normalized uniaxial yield stresses, the values of R, and the normalized elastic moduli, respectively, for the sheet metal after plane-strain compression with the compressive thickness strain of 0.79 at various in-plane orientations with respect to the rolling direction based on definition I. In the figures, Θ represents the angle between the uniaxial tension directions and the rolling direction. The corresponding values based

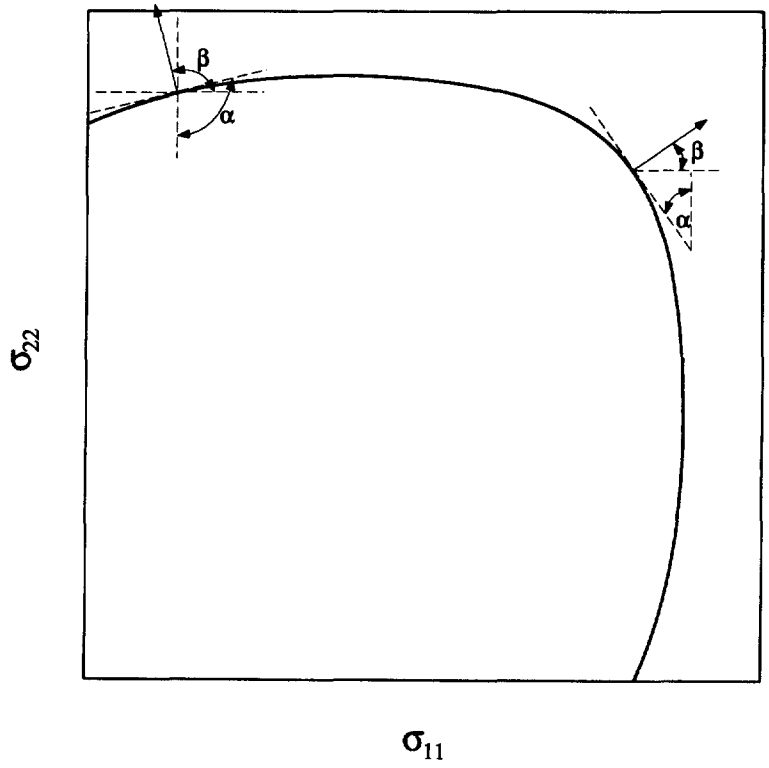

Fig. 20. Representation of the tangent direction of the yield surface and the plastic flow direction.

Table 2. The values of α and β defined in eqns (50) and (51) at various stress ratios based on the $\langle 111 \rangle$ pencil glide system

σ_1/σ_2	0.05	0.1	0.2	0.25	0.33	0.5	0.67	0.71	0.77
α (degree)	117.1	115.2	112.9	110.7	105.9	81.1	71.2	66.2	56.4
β (degree)	117.8	116.4	112.6	110.9	107.8	82.4	66.4	62.3	53.3
σ_1/σ_2	0.83	0.91	1.0	1.1	1.2	1.3	1.4	1.5	2.0
α (degree)	41.9	34.4	28.7	25.7	17.9	13.2	9.7	5.8	4.8
β (degree)	39.7	31.1	24.5	19.7	13.0	9.6	6.9	4.9	2.6
σ_1/σ_2	3.0	4.0	5.0	10.0	20.0				
α (degree)	10.0	17.2	21.8	24.4	26.2				
β (degree)	-9.4	14.1	16.8	21.5	22.9				

on the Hill quadratic yield criterion and the Yld96 yield criterion with $m = 4$ (Barlat, 1997c) are also plotted in Fig. 21(a) and (b). It should be noted that the yield stresses and the values of R at various planar orientations based on the Hosford yield criterion and Hill cubic yield criterion are not shown in Fig. 21(a) and (b) because these two yield criteria require the principal stress directions to coincide with the orthotropic symmetry axes.

Figure 21(a) shows the normalized uniaxial yield stresses based on the simulations at various planar orientations. These yield stresses have a maximum difference of 10%. The yield stresses based on both the Hill quadratic yield criterion and the Yld96 yield criterion with $m = 4$ are in good agreement with those based on the simulations. Figure 21(b) shows the values of R at various planar orientations. Note that the values of R based on the Hill quadratic yield criterion are significantly different from those based on the simulations whereas the values of R based on the Yld96 yield criterion agree well with the simulation results. Figure 21(c) shows the normalized elastic modulus as a function of the planar orientation. Note that the trend of the normalized elastic moduli is similar to that of the normalized yield stresses (as shown in Fig. 21(a)). There is a maximum difference of 15% for the elastic moduli at various planar orientations as shown in the figure. It should be noted that the elastic modulus is an important parameter to determine the springback in sheet forming operations.

4.3.2. $\{110\}\ \langle 111 \rangle$ *slip system* Figure 22 shows the results of the simulated yield surfaces based on the $\{110\}\ \langle 111 \rangle$ slip system and definition I for sheets subjected to in-plane biaxial tension and shear after plane-strain compression with the compressive thickness strain of 0.79. The results of the simulations with no shear give nearly flat contours in Region A and B and a rounded vertex near equal biaxial tension direction in Region B. Figure 22 also shows the results of the simulated yield surfaces for several ratios of the shear stress to the yield stress in the rolling direction. In the figure, the rounded vertex disappears gradually as s increases.

4.3.3. $\{112\}\ \langle 111 \rangle$ *slip system* Figure 23 shows the results of the simulated yield surfaces based on the $\{112\}\ \langle 111 \rangle$ slip system and definition I for sheets subjected to in-plane biaxial tension and shear after plane-strain compression with the compressive thickness strain of 0.79. As shown in the figure, when the shear stress is zero, there are two relatively inflated parts of the simulated yield surface in both Region A and B. Figure 23 also shows the results of the simulated yield surfaces for several ratios of the shear stress to the yield stress in the rolling direction. In the figure, the shapes of the simulated yield surfaces based on the $\{112\}\ \langle 111 \rangle$ slip system, contrary to those based on the $\{110\}\ \langle 111 \rangle$ slip system, show a rounded vertex near equal biaxial tension direction as the shear stress ratio s increases. As s decreases, the yield surfaces become close to each other in the equal biaxial tension direction.

Finally, the simulated yield surfaces (without in-plane shear stresses) based on the three slip systems are redrawn in Fig. 24. Note that the yield stresses are normalized individually by the uniaxial yield stresses in the rolling direction based on the three slip

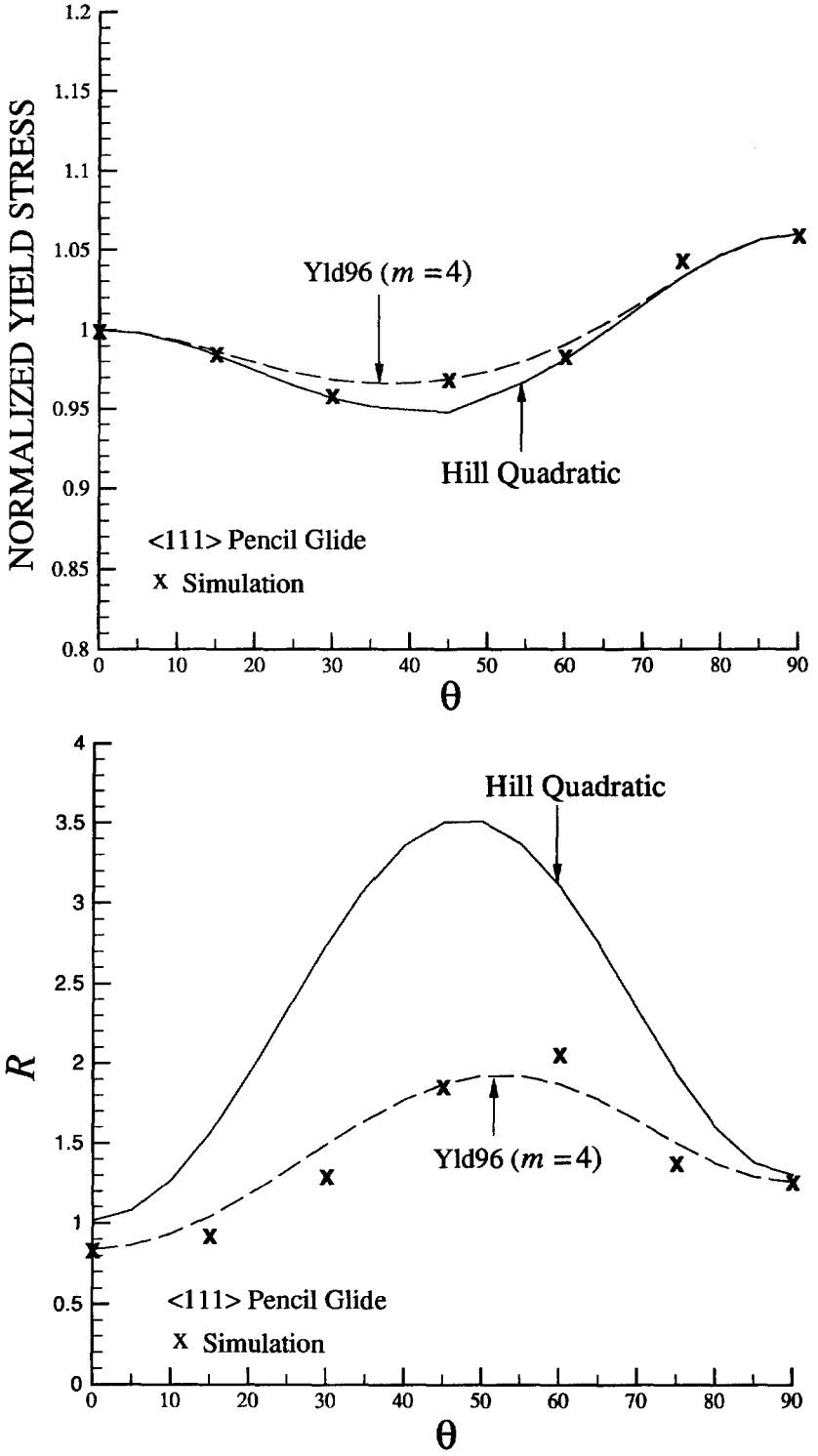

Fig. 21. (a) The normalized uniaxial stresses, (b) the values of R and (c) the normalized elastic moduli at various orientations with respect to the rolling direction obtained from the simulations based on the $\langle 111 \rangle$ pencil glide system and definition I compared with those based on the Hill quadratic yield criterion and the Yld96 yield criterion with $m = 4$ for sheets after plane-strain compression with the compressive thickness strain of 0.79.

systems. The three simulated yield surfaces show different shapes in the figure. As reported in Viana *et al.* (1979), the simulated yield surfaces based on the $\langle 111 \rangle$ pencil glide system show a smoother contour than those based on restricted slip systems.

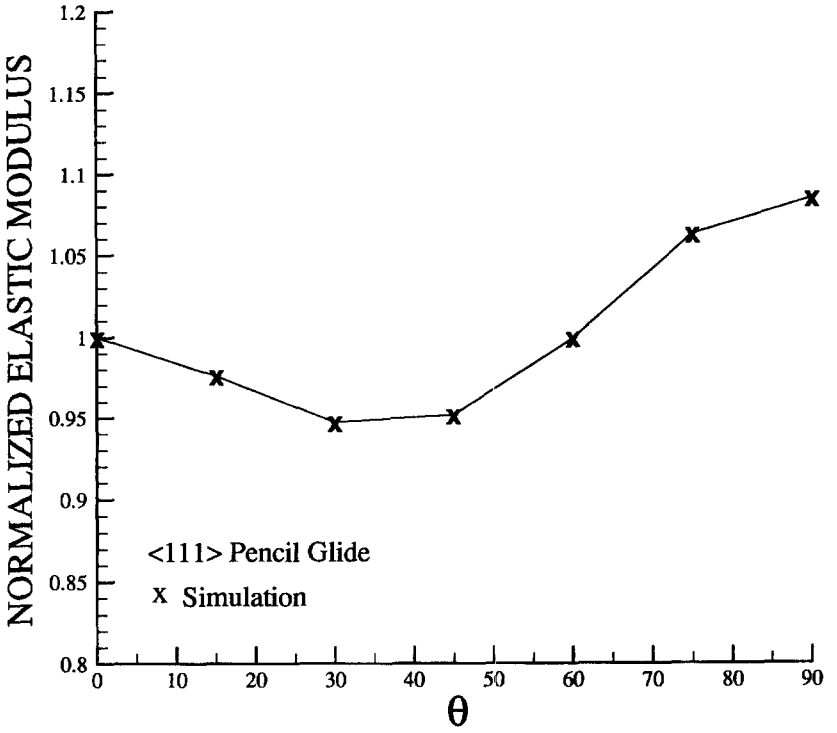

Fig. 21.—*Continued.*

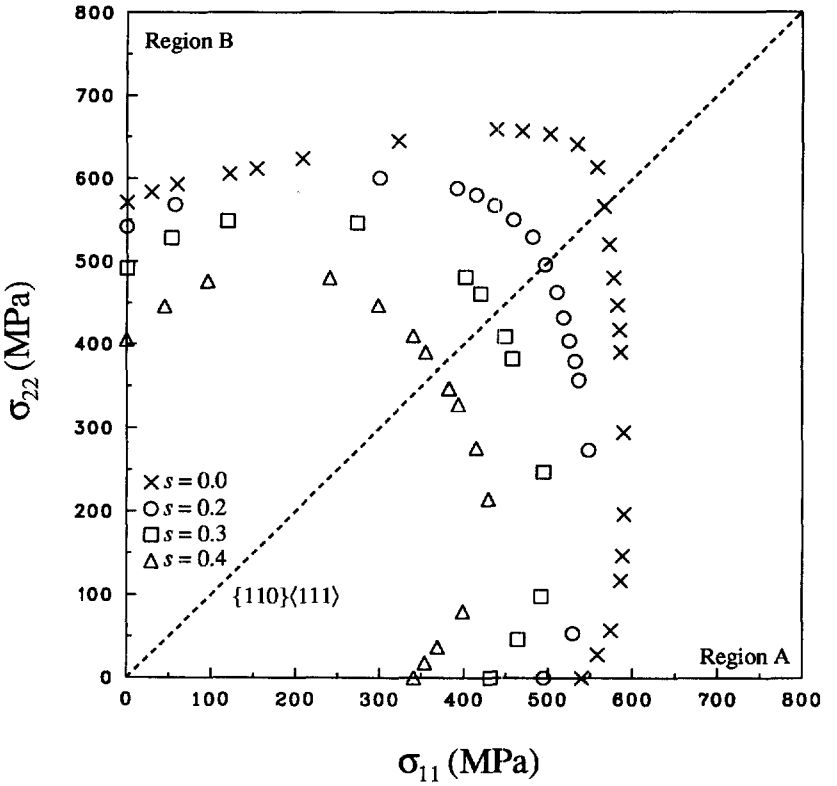

Fig. 22. The results of the simulated yield surfaces for the shear stress ratio ($\sigma_{12}/\bar{\sigma} \equiv s$) of 0, 0.2, 0.3, and 0.4 based on the {112} ⟨111⟩ slip system and definition I for sheets after plane-strain compression with the compressive thickness strain of 0.79.

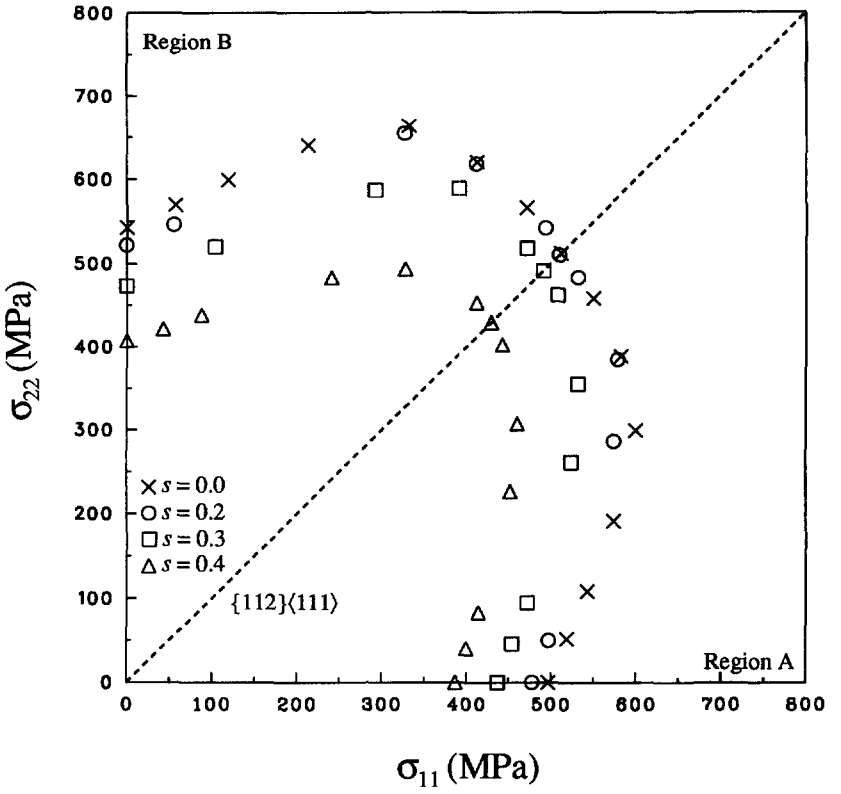

Fig. 23. The results of the simulated yield surfaces for the shear stress ratio ($\sigma_{12}/\bar{\sigma} \equiv s$) of 0, 0.2, 0.3, and 0.4 based on the {112} ⟨111⟩ slip system and definition I for sheets after plane-strain compression with the compressive thickness strain of 0.79.

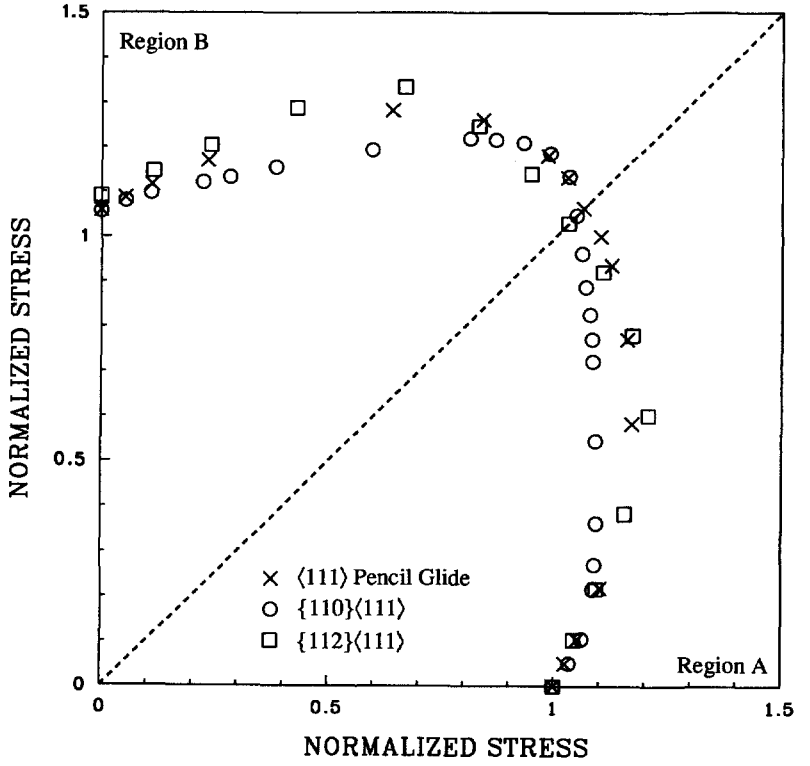

Fig. 24. The results of the simulated yield surfaces based on definition I and the ⟨111⟩ pencil glide, {110} ⟨111⟩, and {112} ⟨111⟩ slip systems for sheets after plane-strain compression with the compressive thickness strain of 0.79.

5. CONCLUSIONS

The Taylor-like polycrystal model of Asaro and Needleman (1985) and some formulations of Bronkhorst *et al.* (1992) are adopted here to investigate the plastic behavior of a b.c.c. low-carbon steel under plane-strain compression and the subsequent in-plane loading conditions. The $\langle 111 \rangle$ pencil glide system is considered as the main slip mechanism. The $\{110\}\ \langle 111 \rangle$ and $\{112\}\ \langle 111 \rangle$ slip systems are also considered. Our computational results indicate that the pole figures for the b.c.c. steel after plane-strain compression are not strongly dependent upon the slip system selected. Also the pole figures at large compressive plastic strains agree with the corresponding experimental results. The yield surfaces based on the $\langle 111 \rangle$ pencil glide system under biaxial stretching conditions from the simulations depend upon the amount of plastic work. The yield stresses and the R values from the simulations at various in-plane orientations can be fitted by a generalized yield function of Barlat *et al.* (1997b) where the yield stresses and the R values in the rolling, transverse and the 45° directions as well as the yield stress under equal biaxial tension are needed as the input for determination of the yield function. Finally, the yield surfaces from the simulations indicate that the yield surfaces strongly depend upon the slip system selected in the simulations.

Acknowledgements—The authors acknowledge the support of this work by the National Science Foundation under grant number DDM-9102424 and the University Research Program of Ford Motor Company. Helpful discussions with Professor W. F. Hosford of the University of Michigan during the course of this investigation are greatly appreciated. The authors also express deep appreciation to Dr. F. Barlat for providing the results based on the new generalized yield function.

REFERENCES

Asaro, R. J. and Needleman, A. (1985) Texture development and strain hardening in rate dependent polycrystals. *Acta Metallica* **33,** 923–953.

Asaro, R. J. and Rice, J. R. (1977) Strain localization in ductile single crystals. *Journal of Mechanics and Physics of Solids* **25,** 309–338.

Barlat, F. and Chung, K. (1993) Anisotropic potentials for plastically deforming metals. *Modelling Simul. Mater. Sci. Eng.* **1,** 403–416.

Barlat, F. and Lian, J. (1989) Plastic behavior and stretchability of sheet metals. Part I: A yield function for orthotropic sheets under plane stress conditions. *International Journal of Plasticity* **5,** 51–66.

Barlat, F., Lege, D. J. and Brem, J. C. (1991) A six-component yield function for anisotropic materials. *International Journal of Plasticity* **7,** 693–712.

Barlat, F., Becker, R. C., Hayashida, Y., Maeda, Y., Yanagawa, M., Chung, K., Brem, J. C., Lege, D. J., Matsui, K., Murtha, S. J. and Hattori, S. (1997a) Yielding description for solution strengthened aluminum alloys. *International Journal of Plasticity*, to appear.

Barlat, F., Maeda, Y., Chung, K., Yanagawa, M., Brem, J. C., Hayashida, Y., Lege, D. J., Matsui, K., Murtha, S. J., Hattori, S., Becker, R. C. and Makosey, S. (1997b) Yield function development for aluminum alloy sheets. *Journal of Mechanics and Physics of Solids*, to appear.

Barlat, F. (1997c) Private communication.

Baudoin, A. J., Bryant, J. D., Dawson, P. R. and Mika, D. P. (1996) Incorporating crystallographic texture in finite element simulations of sheet forming. NUMISHEET '96, ed. J. K. Lee, G. L. Kinzel and R. H. Wagoner, pp. 17–24. The Ohio State University.

Baudoin, A. J., Dawson, P. R., Mathur, K. K., Kocks, U. F. and Korzekwa, D. A. (1994) Application of polycrystal plasticity to sheet forming. *Comp. Methods Appl. Mech. Engrg* **117,** 49–70.

Becker, R. C. (1993) Simulations of earing in aluminum single crystals and polycrystals. *Modelling Simul. Mater. Sci. Eng.* **1,** 203–224.

Bishop. J. F. W. and Hill, R. (1951a) A theory of the plastic distortion of a polycrystalline aggregate under combined stresses. *Philosophical Magazine* **42,** 414–427.

Bishop. J. F. W. and Hill, R. (1951b) A theoretical derivation of the plastic properties of a polycrystalline face-centred metal. *Philosophical Magazine* **42,** 1298–1307.

Bronkhorst, C. A., Kalidindi, S. R. and Anand, L. (1992) Polycrystal plasticity and the evolution of crystallographic texture in face-centered cubic metals. *Phil. Trans. R. Soc. Lond.* **A341,** 443–477.

Bunge, H. J. (1982) *Texture Analysis in Material Science—Mathematical Methods.* Butterworth, London.

Ceccalid, D., Yala, F., Baudin, T., Penelle, R., Royer, F. and Arminjon, M. (1994) Deformation textures and plastic anisotropy and steels using the Taylor and non-homogeneous models. *International Journal of Plasticity* **10,** 643–661.

Dillamore, I. L., Hazel, R. J., Watson, T. W. and Hadden, P. (1971) An experimental study of the mechanical anisotropy of some common metals. *Int. J. Mech. Sci.* **13,** 1049–1061.

Friedman, P. A., Liao, K.-C., Pan, J. and Barlat, F. (1997) Texture development and hardening characteristics of steel sheet during cold rolling, manuscript being prepared.

Ghosh, A. K. and Hecker, S. S. (1975) Failure in thin sheets stretched over rigid punches. *Metall. Trans.* **6A,** 1065–1074.

Gilormini, P. (1989) The theory of rate sensitive pencil glide application to rolling textures. *Acta Metallica* **37,** 2093–2101.

Gotoh, M. (1977) A theory of plastic anisotropy based on a yield function of fourth order (plane stress state)—I and II. *Int. J. Mech. Sci.* **19,** 505–520.

Hecker, S. S. (1976) Experimental studies of yield phenomena in biaxially loaded metals. *Constitutive Equations in Viscoplasticity: Computational and Engineering Aspects*, ed. A. Stricklin and K. C. Saczalski, pp. 1–33. ASME, New York.

Hershey, A. V. (1954) The plasticity of an isotropic aggregate of anisotropic face-centered cubic crystals. *Journal of Applied Mechanics* **21,** 241–249.

Hill, R. (1948) A theory of the yielding and plastic flow of anisotropic metals. *Proceedings of the Royal Society of London* **A193,** 281–297.

Hill, R. (1972) On constitutive macro-variables for heterogeneous solids at finite strain. *Proceedings of the Royal Society of London* **A326,** 131–147.

Hill, R. (1979) Theoretical plasticity of textured aggregates. *Math. Proc. Camb. Phil. Soc.* **85,** 179–191.

Hill, R. (1990) Constitutive modeling of orthotropic plasticity in sheet metals. *Journal of Mechanics and Physics of Solids* **38,** 405–417.

Hill, R. (1993) A user-friendly theory of orthotropic plasticity in sheet metals. *Int. J. Mech. Sci.* **35,** 19–25.

Hosford, W. F. (1979) On yield loci of anisotropic cubic metals. *Proceedings of the 7th North American Metalworking Conference*, pp. 191–197. SME, Dearborn, Michigan.

Hosford, W. F. (1996) On the crystallographic basis of yield criteria. *Textures and Microstructures* **26–27,** 479–493.

Hutchinson, J. W. (1964) Plastic deformation of b.c.c. polycrystals. *Journal of Mechanics and Physics of Solids* **12,** 25–33.

Kalidindi, S. R., Bronkhorst, C. A. and Anand, L. (1992) Crystallographic texture evolution in bulk deformation processing of fcc metals. *Journal of Mechanics and Physics of Solids* **40,** 537–569.

Karafillis, A. P. and Boyce, M. C. (1993) A general anisotropic yield criterion using bounds and a transformation weighting tensor. *Journal of Mechanics and Physics of Solids* **41,** 1859–1886.

Keh, A. S. (1965) Work hardening and deformation sub-structure in iron single crystals deformed in tension at 298°K. *Philosophical Magazine* **12,** 9–30.

Lee, E. H. (1969) Elastic–plastic deformation at finite strains. *Journal of Applied Mechanics* **36,** 1–6.

Lee, J. K., Kinzel, G. L. and Wagoner, R. H. (1996) *NUMISHEET* '96. The Ohio State University.

Lin, S. B. and Ding, J. L. (1996) A modified form of Hill's orientation-dependent yield criterion for orthotropic sheet metals. *Journal of Mechanics and Physics of Solids* **44,** 1739–1764.

Logan, R. W. and Hosford, W. F. (1980) Upper-bound anisotropic yield locus calculations assuming ⟨111⟩-pencil glide. *Int. J. Mech. Sci.* **22,** 419–430.

Mathur, K. K. and Dawson, P. R. (1989) On modeling the development of crystallographic texture in bulk forming processes. *International Journal of Plasticity* **5,** 67–94.

Nakada, Y. and Keh, A. S. (1966) Latent hardening in iron single crystals. *Acta Metallica* **14,** 961–973.

Pan, J. and Rice, J. R. (1983) Rate sensitivity of plastic flow and implications for yield-surface vertices. *International Journal of Solids and Structures* **19,** 973–987.

Peirce, D., Asaro, R. J. and Needleman, A. (1982) An analysis of nonuniform and localized deformation in ductile single crystals. *Acta Metallica* **30,** 1087–1119.

Peirce, D., Shih, C. F. and Needleman, A. (1984) A tangent modulus method for rate dependent solids. *Comp. Struct.* **18,** 875–887.

Segmüller, A. and Wassermann, G. (1960) Walztexturen von Molybdän und Tantal. *Freiberger Forschungshefte* **B38,** 38.

Smithells Metals Reference Book (1983) 6th edn, ed. E. A. Brandles. Butterworth, London.

Taylor, G. I. and Elam, C. F. (1923) The distortion of an aluminum crystal during a tensile test. *Proceedings of the Royal Society of London* **A102,** 643–667.

Taylor, G. I. (1938) Plastic strain in metals. *J. Inst. Metals* **62,** 307–324.

Taylor, G. I. (1955) Strains in crystalline aggregates. *Proceedings of the Colloquium on Deformation and Flow of Solids* (Madrid, 1955), 586–593.

Viana, C. S. da C., Kallend, J. S. and Davies, G. J. (1979) The use of texture data to predict the yield locus of metal sheets. *Int. J. Mech. Sci.* **21,** 355–371.

Wang, N. M. and Wenner, M. L. (1978) Elastic–viscoplastic analyses of simple stretch forming problems. In *Mechanics of Sheet Metal Forming*, ed. D. P. Koistinen and N. M. Wang, pp. 367–402. Plenum Press, New York.

Yang, S. and Bacroix, B. (1996) Shear banding in strain hardening polycrystals during rolling. *International Journal of Plasticity* **12,** 1257–1285.